Applied Catalysis B: Environmental 259 (2019) 118062

Contents lists available at ScienceDirect

Applied Catalysis B: Environmental

journal homepage: www.elsevier.com/locate/apcatb

Uncovering the mechanism of novel $AgInS_2$ nanosheets/TiO_2 nanobelts composites for photocatalytic remediation of combined pollution

Jinge Du[a,b], Shuanglong Ma[c,*], Haiping Liu[a], Haichao Fu[c], Li Li[a], Zhuoqian Li[c], Yi Li[c], Jianguo Zhou[a,d,*]

[a] School of Environment, Key Laboratory of Yellow River and Huai River Water Environment and Pollution Control (Ministry of Education), Henan Engineering Laboratory of Environmental Functional Materials and Pollution Control, Henan Normal University, Xinxiang, 453007, China
[b] Department of Chemistry, Sanquan College of Xinxiang Medical University, Xinxiang 453003, China
[c] College of Resources and Environmental Sciences, Henan Agricultural University, Zhengzhou 450002, China
[d] Key Laboratory of Green Chemical Media & Reactions (Ministry of Education), Xinxiang 453007, China

ARTICLE INFO

Keywords:
$AgInS_2$
TiO_2
Cr(VI) reduction
Photocatalytic disinfection
BPA degradation

ABSTRACT

In this work, a novel $AgInS_2$ nanosheets/TiO_2 nanobelts photocatalyst was prepared by a facile hydrothermal method. The $AgInS_2$/TiO_2 with the optimal ration showed excellent photocatalytic performance in simultaneous *Escherichia coli* (*E. coli*) disinfection and Cr(VI) reduction or *E. coli* disinfection and bisphenol A (BPA) degradation. The superior photocatalytic effect were possibly attributed to formation of heterojunction between $AgInS_2$ nanosheets and TiO_2 nanobelts, which could increase the absorption of visible light, facilitate the separation of photo-induced carrier and held the redox of photo-generated e^- and h^+. The production of reactive species during the disinfection process was also investigated by employing chemical scavengers, electron spin resonance, and spectroscopy technique, revealing the paramount role of h^+ and O_2•–. This study paves a new way to rationally design the novel TiO_2 nanobelts or $AgInS_2$ nanosheets based photocatalysts for combined pollution remediation in water environment.

1. Introduction

Water contamination with pathogenic microorganisms have threatened public health with more than two million deaths caused by pathogen-contaminated water every year [1,2]. Many disadvantages can be found in the traditional bactericidal applications including the generation of carcinogenic disinfection by-products with chlorination [3], inferior effect toward rotavirus, hepatitis A, or adenovirus with UV irradiation disinfection [4], and the existence of poisonous bromate with ozone disinfection [5]. Therefore, it is significant and urgent to develop a highly efficient, cost-effective, and eco-friendly disinfection technology [6]. Since it was first discovered by Matsunaga [7], photocatalytic disinfection have drawn much attention with popular and extensive research around the world. Due to its utilization of abundant solar energy, easy operation, no disinfection by-products, photocatalytic disinfection was considered as one of the most promising candidates for sustainable disinfection technologies.

Among various semiconductor photocatalysts, TiO_2 has been widely applied in photocatalytic disinfection due to its nontoxic, inexpensive and chemical stability. Different morphologies of TiO_2 including nanoparticles [8], nanobelts [9] and microspheres [10] have been prepared and applied in disinfection. Among which, one-dimensional (1D) TiO_2 nanomaterials have aroused great attention due to their high aspect ratio, great electron mobility and high surface-to-volume ratio compared to bulk counterparts [11,12]. Wang et al. discovered that Ag/acid-corroded TiO_2 nanobelts exhibited good antibacterial effect [13]. However, the photoactivity of TiO_2 is limited to ultraviolet light region due to the large band gaps of 3.15 eV, which restricts its application. Therefore, it is important to broaden the light absorption range of 1D TiO_2 nanomaterials and thereby enhance their absorption of visible light.

Several strategies have been devoted to enhance the photocatalytic activity of TiO_2 under visible light, such as nonmetal doping [14], noble metal deposition [15], coupling with other narrow-band-gap semiconductors [16,17] and so on. $AgInS_2$, as an important ternary chalcogenide of narrow-band-gap semiconductors, has a distinctive absorption in visible light region due to its narrow-band-gap (1.87–2.03 eV) [18]. Meanwhile, for orthorhombic $AgInS_2$, InS_4 and AgS_4 tetrahedra form a wurtzite-like structure in the unit cell. And the distortion of tetrahedra, which produced by the unequal bonds of AgS

* Corresponding authors.
E-mail addresses: shuanglongma168@163.com (S. Ma), zhoujgwj@163.com (J. Zhou).

https://doi.org/10.1016/j.apcatb.2019.118062
Received 1 May 2019; Received in revised form 20 July 2019; Accepted 6 August 2019
Available online 10 August 2019
0926-3373/

and InS, would be beneficial to the formation of internal electric field. Therefore, the charge can be separated rapidly under illumination leading the improvement of photocatalytic activity [19]. To the best of our knowledge, matched band positions of TiO_2 and $AgInS_2$ can produce a heterojunction, which can expand light absorption range and promote charge separation. At the current stage, several researches of $AgInS_2/TiO_2$ have been done in order to remediate water environment. For example, Liu et al. reported that $AgInS_2/TiO_2$ heterojunction prepared by a facile hydrothermal method achieved much enhanced visible light photoactivity for the degradation of gaseous 1, 2-dichlorobenzene [20]. Zhang et al. and Cui et al. prepared $AgInS_2$ nanoparticles deposited onto TiO_2 nanotube arrays and studied their photoelectrocatalytic activity for degradation of norfloxacin and methyl orange [21,22]. From these studies, it is obvious that the heterojunction constructed by coupling $AgInS_2$ and TiO_2 can significantly improve the catalytic performance. However, the $AgInS_2$ nanosheets/TiO_2 nanobelts used as photocatalyst in control of combined pollution of pathogenic bacteria and heavy metal or pathogenic bacteria and emerging pollutant has not been reported. Therefore, it is meaningful to design a novel $AgInS_2$ and TiO_2 composite with high photocatalytic activity for combined pollution remediation.

In this paper, we developed a strategy for design and fabricate novel $AgInS_2$ nanosheets/TiO_2 nanobelts ($AgInS_2/TiO_2$) via a two-step hydrothermal method. The $AgInS_2$ nanosheets were successfully precipitated on the surfaces of TiO_2 nanobelts by self-assembly. Subsequently, the as-synthesized $AgInS_2/TiO_2$ were first used as biocides against *E. coli* under solar light irradiation. The effect of environmental factors such as temperature, humic acid and inorganic anions on disinfection efficiency of *E. coli* were discussed. Meanwhile, Cr(VI) and BPA were used to assess the reduction and degradation performance of photocatalyst. The photocatalytic activity of $AgInS_2/TiO_2$ was further demonstrated by simultaneous remediation of *E. coli* and Cr(VI) or *E. coli* and BPA contaminated water. The morphologies, structures, specific surface areas, optical properties of photocatalysts were characterized using FESEM, TEM, XRD, BET, XPS and UV–vis analysis. Furthermore, the proposed mechanism was investigated using PL, photoelectrochemical experiments, EPR spectra and radical trapping experiments.

2. Experimental section

2.1. Chemical reagents

Sodium hydroxide (NaOH), silver nitrate ($AgNO_3$), potassium dichromate ($K_2Cr_2O_7$), indium nitrate hydrate ($In(NO_3)_3{\cdot}4.5H_2O$), thioacetamide (TAA), 3-mercaptopropionic acid (MPA), terephthalic acid (TA), titanium oxysulfate ($TiOSO_4$), 5,5-dimethyl-1-pyrroline N-oxide (DMPO) and nitrotetrazolium blue chloride (NBT) were purchased from Aladdin Industrial Co. Ltd., China., and commercial grade P25 was purchased from Degussa. All chemical reagents were reagent grade without further purifications.

2.2. Preparation of TiO_2 nanobelts

TiO_2 nanobelts were prepared via a hydrothermal method [23]. 0.8 g P25 was dispersed in 80 mL NaOH solution (10 M), and magnetically stirred for 1 h. Then the miscible liquid was transferred into 100 mL Teflon liner, followed by heated at 180 °C for 48 h. The resulting sample was rinsed with deionized water and then dispersed in 0.1 M HCl solution for 24 h. Subsequently, the precipitate was washed several times with deionized water until neutral pH and dried at 60 °C for 24 h. Finally, the precipitate was annealed for 4 h at 500 °C for crystallization of TiO_2 nanobelts.

2.3. Preparation of $AgInS_2$ nanosheets/TiO_2 nanobelts

The $AgInS_2$ nanosheets/TiO_2 nanobelts were prepared by a hydrothermal method. First, 0.1 g TiO_2 nanobelts were added to 16 mM 3-mercaptopropionic acid aqueous solution (70 mL) under vigorous stirring for 2 h. Subsequently, different amounts of $AgNO_3$, $In(NO_3)_3$ and TAA at a molar ratio of 1:1:2 were individually added to the TiO_2 suspension to obtain different molar ratios (0.1:1, 0.3:1, 0.5:1, and 0.7:1) of $AgInS_2$ to TiO_2. After stirring for 20 min, the above solution was adjusted to pH of 10.6 with NaOH solution. The obtained brown mixture was transferred to a 100 mL Teflon liner, which was held at 180 °C for 24 h. The final product was centrifuged, rinsed with deionized water several times, and then dried at 60 °C for 24 h. Afterwards, the corresponding samples were denoted as 0.1AT, 0.3AT, 0.5AT and 0.7AT, respectively. For comparison, pristine $AgInS_2$ was prepared with the same condition as $AgInS_2/TiO_2$, except that TiO_2 nanobelt was absence.

2.4. Photocatalyst characterization

FESEM and TEM images were recorded using field-emission scanning electron microscopy (FESEM, SU8010) and transmission electron microscope (HRTEM, JEM-2100), respectively. Energy-dispersive X-ray spectroscopy (EDS) was performed by a FEI (Tecnai G2 F20) instrument equipped with an energy dispersive spectroscopy. X-ray diffraction (XRD) measurements were carried out using an X-ray diffractometer (Bruker D8 Advance) with a Cu Kα radiation. Zeta potential of TiO_2 nanobelts in aqueous phase was measured using a Zetasizer Nano instrument (Malvern Instruments, UK). BET specific surface area measurements were examined by N_2 adsorption-desorption using an MicrotracBEL instrument. XPS spectra were obtained using an AXIS-Ultra spectrometer (Kratos). UV–vis diffuse reflection spectra (UV–vis DRS) were recorded on a Lambda 950 spectrometer in the region of 200–800 nm, using $BaSO_4$ as the reflectance standard. Three-dimensional excitation-emission matrix fluorescence spectra (3D EEMs) were conducted with a F-4600 spectrofluorimeter. The photocurrent, electrochemical impedance spectroscopy (EIS) and Mott-Schottky plots were recorded on an electrochemical workstation (CHI-660E) with a three-electrode system in 1 mol/L Na_2SO_4 solution. Photoluminescence spectra (PL) were recorded by F-4600 fluorescence spectrometer at room temperature.

2.5. Photocatalytic activity

2.5.1. Photocatalytic inactivation test of bacteria

E. coli (ATCC 44752), a common waterborne bacterium in drinking water, was chosen as model bacteria to study the photocatalytic disinfection activity of as-prepared samples. The bacteria were inoculated in nutrient broth and cultured at 37 °C with 180 rpm for 15 h until the cell concentration reached $10^{9.0}$ colony forming units (cfu)/mL. Then the cells were diluted with sterilized NaCl (0.85%) solution to $10^{7.2}$ cfu/mL for disinfection experiments. 250 μL catalyst solution (4 mg/L) was dispersed in 10 mL of *E. coli* suspension. The experimental device was shown in Fig. S1. All the photocatalytic experiments were conducted by a 300 W Xe lamp (CEL-HXF300, Ceaulight, Beijing, China) as the light source. The wavelength range of the Xe lamp was 325–845 nm (maximum around 382 nm). The light intensity was fixed at 200 mW/cm^{-2}. The spectral analysis of the Xenon arc lamps was shown in Fig. S2. During the inactivation process, the mixture was pipetted out at designated time interval and the bacteria concentration was measured using standard plate count method. The colonies were enumerated by visual inspection after being incubated at 37 °C for 24 h. In addition, the toxicity of materials was discussed in the dark at the same situations for comparison, and the influence of light were measured without the photocatalysts. All the disinfection experiments were repeated three times.

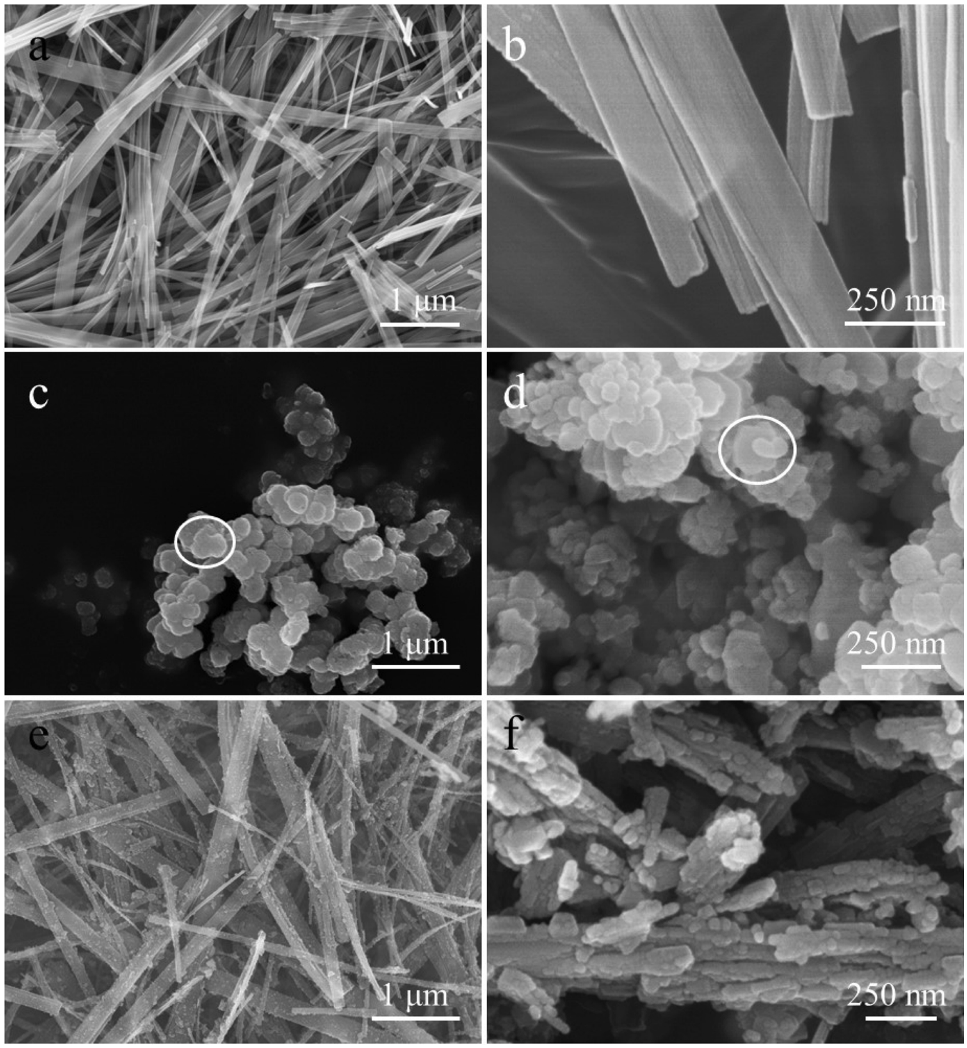

Fig. 1. FESEM image of (a, b) TiO_2, (c, b) $AgInS_2$, (e, f) $AgInS_2/TiO_2$ composite.

2.5.2. Photocatalytic reduction of Cr(VI)

For individual Cr(VI) reduction, a certain amount of catalyst was added to 20 mL Cr(VI) (5 mg/L, 1.2 mM citric acid) solution. The solution was stirred for 40 min in the dark to reach the adsorption/desorption equilibrium. At regular time intervals, 2 mL suspension was microfiltered with a 0.22 μm hydrophilic membrane. Cr(VI) concentration was measured by a UV–vis spectrometer (UV-2100, SHIMADU) according to the reported method by Dozzi [24]. The detailed method was shown in Supplementary Material.

2.5.3. Photocatalytic remediation of E. coliand Cr(VI) combined pollution

200 μL Cr(VI) (500 mg/L) and a certain amount of catalyst were added to 20 mL bacterial solution ($10^{7.2}$ cfu/mL). Then the mixed solution was stirred in the dark for 40 min to reach the adsorption/desorption equilibrium between the photocatalyst and pollutants. At regular intervals, the bacteria were counted using the standard plate count method, and the Cr(VI) was detected by a UV–vis spectrometer. All the experiments were repeated three times.

2.5.4. Photocatalytic degradation of BPA

The concentration of photocatalyst and BPA was 100 μg/mL and 10 mg/L, respectively. Prior to irradiation, the suspension was stirred for 45 min in the dark to obtain the adsorption-desorption equilibrium. At given irradiation time intervals, 0.8 mL suspension was taken out and microfiltered with a 0.22 μm hydrophilic membrane to separate the photocatalyst. The BPA concentration was determined by high-performance liquid chromatography (HPLC, Ultimate 3000) equipped with a UV detector and C18 column. The mobile phase was 50% acetonitrile and 50% water (with 0.1% formic acid) with a flow rate of 0.8 mL/min.

2.5.5. Photocatalytic remediation of E. coli and BPA combined pollution

The concentration of photocatalyst, BPA and *E. coli* was 100 μg/mL, 10 mg/L and $10^{7.2}$ cfu/mL, respectively. The suspensions were magnetically stirred under dark for 40 min to reach the adsorption-desorption equilibrium. At designated time intervals, the bacteria were counted using the standard plate count method, and the BPA was detected by HPLC.

2.6. Microscopic observations of bacteria

The interaction between *E. coli* and photocatalysts was studied by field-emission scanning electron microscopy. First, the photo-treated bacteria were dropped on a silicon pellet and were fixed with 2.5% glutaraldehyde solution at 4 °C overnight. Then, the samples were dehydrated via ethanol solutions (30%, 50%, 70%, 90% and 100%, respectively) for 20 min. Finally, the lyophilized specimens were sputter-coated with gold and observed on Hitachi SU8010. For uncovering the *E. coli* death tendency under solar light irradiation from 0 min to 180 min, fluorescent-based cell live/dead test were carried out. The treated mixture was stained with propidium iodide (PI) and SYTO9

(LIVE/DEAD Baclight Bacterial Viability kit) for 20 min. The stained bacterial suspensions were imaged using a Leica TCS SP8 laser scanning fluorescence microscopy.

2.7. Reactive species analyses

EPR spectra of $^{\cdot}OH$ and $O_2^{\cdot}$– trapped by DMPO were recorded by a Bruker EMS-plus EPR. 0.5 mM Isopropyl alcohol (IPA), 0.5 mM sodium oxalate, 0.01 mM p-benzoquinone (BQ), 0.1 mM Fe(II)-EDTA, 0.05 mM Cr(VI) were served as scavengers for $^{\cdot}OH$, h^+, $O_2^{\cdot}$–, H_2O_2, and e^-, respectively. TA (0.25 mM in a 1 mM NaOH solution) could react with $^{\bullet}OH$ to produce 2-hydroxyterephthalic acid, which could be detected using a Hitachi F-4600 fluorescence spectrophotometer [25]. 2.5×10^{-5} M NBT was used to detect the amount of $O_2^{\cdot}$–. The production of $O_2^{\cdot}$– which was quantitatively analyzed by detecting the concentration of NBT with Shimadzu UV-2100 spectrophotometer (absorption maximum at 259 nm) [26]. $TiOSO_4$ was used to detect H_2O_2 according to the reported method by Xia [27].

3. Results and discussion

3.1. Characterization

Fig. 1a, b revealed that the pure TiO_2 had a smooth surface with diameters around 200 nm and lengths of several micrometers. The $AgInS_2$ (Fig. 1c, d) exhibited uniform nanosheet structures with the diameters around 200 nm. After the hydrothermal deposition of $AgInS_2$, the diameter of TiO_2 nanobelts became large and the outer surfaces became rough (Fig. 1e, f). This phenomenon was attributed to that the $AgInS_2$ nanosheets with high coverage density were grown on the surface of TiO_2, which was expected to facilitate the efficient separation of photoinduced e^--h^+ pairs during the photocatalytic reaction.

TEM of pristine TiO_2 was shown in Fig. 2a. TiO_2 had a morphology of regular and smooth nanobelt with diameters around 200 nm, which was consistent with the SEM result. The lattice spacings of 0.623 and 0.356 nm in the HRTEM image were ascribed to the distances of (001) and (110) crystallographic plane of TiO_2, respectively (Fig. 2b). The lattice defects were observed clearly in TiO_2 (inset of Fig. 2b), confirming the defect formation during the fabrication process of TiO_2 nanobelts [28]. As shown in Fig. 2c, a clear nanosheet structure could be observed for bare $AgInS_2$. The lattice fringes of $AgInS_2$ were 0.310 and 0.242 nm, which were corresponded to the (201) and (122) plane of $AgInS_2$ nanosheets, respectively (Fig. 2d). According to TEM image of 0.5AT (Fig. 2e), the heterojunction by integrating of nanobelts with nanosheets were successfully developed. The HRTEM image of 0.5AT revealed that the interplanar spacings of 0.623 and 0.356 nm were ascribed to the (001) and (110) plane of TiO_2, and 0.310 nm was attributed to the (201) plane of $AgInS_2$ (Fig. 2f). As the inset of Fig. 2f, the lattice defects of TiO_2 were retained after the hydrothermal process for composites, demonstrating that the $AgInS_2$ deposition process had little influence on the structure of TiO_2. Some studies revealed that defect could extend the light absorbance and enhance photocatalytic activity [29]. These observations manifested that the heterojunction with highly crystalline were successfully obtained. Fig. 2g was a representative TEM image of 0.5AT with a corresponding EDS elemental mapping of Ti, O, Ag, In and S shown in Fig. 2h-l. The Ti element was virtually identical with O element with continuous and concentrating distribution, resembling the morphology of TiO_2 nanobelts. In contrast, the distributions of Ag, In and S elements were discontinuous, suggesting the discrete distribution of $AgInS_2$ on the TiO_2 nanobelts. These analyses demonstrated that $AgInS_2/TiO_2$ heterojunction had been successfully synthesized and the intimate contact existed between TiO_2 and $AgInS_2$.

As shown in Fig. 3a, the survey spectra clearly indicated the presence of Ti and O elements in TiO_2 nanobelt, Ag, In, and S in $AgInS_2$ nanosheet, and all above elements in $AgInS_2/TiO_2$ composites. For the Ti 2p spectrum of TiO_2 in Fig. 3b, two characteristic peaks of 458.41 and 464.10 eV correspond to Ti $2p_{3/2}$ and Ti $2p_{1/2}$, respectively, suggesting that the valence states of Ti was 4+ [30]. Typically, two characteristic peaks of Ti^{4+} in the all $AgInS_2/TiO_2$ composites shifted toward higher values compared to bare TiO_2 (Fig. 3b). Although Ti^{3+} was observed in pure TiO_2 using EPR spectroscopy (Fig. 10c), no peaks of Ti^{3+} $2p_{1/2}$ at 463.8 eV and Ti^{3+} $2p_{3/2}$ at 458.8 eV were observed in XPS spectra of TiO_2 and $AgInS_2/TiO_2$ composites [31]. This might be attributed to the deep state or low amounts of Ti^{3+} on TiO_2, which was hard to detect by XPS technique [32]. From Fig. 3c, O 1s of TiO_2 could be deconvoluted to Ti-O at 529.78 eV and surface −OH species at 530.95 eV [33]. For $AgInS_2/TiO_2$ composites, the binding energies of O 1s also shifted to higher values compared to TiO_2, which was consistent with the result of Ti^{4+}. Moreover, these Ti and O shifts became more obvious with the increase of $AgInS_2$ amount. In terms of the Ag 3d spectrum of $AgInS_2$ (Fig. 3d), intensive signals at 368.18 and 374.19 eV was assigned respectively to Ag $3d_{5/2}$ and Ag $3d_{3/2}$, which demonstrated the existence of Ag^+ in the composite. From the In 3d spectrum of $AgInS_2$ in Fig. 3e, the peaks at 452.59 and 445.04 eV were ascribed to In $3d_{3/2}$ and In $3d_{5/2}$, respectively. Furthermore, two peaks at 161.75 and 162.98 eV were attributed to S 2p in $AgInS_2$ (Fig. 3f). The binding energies of Ag 3d, In 3d and S 2p for $AgInS_2/TiO_2$ composites all showed negative shift compared with those of pure $AgInS_2$, and this shift phenomenon became less obvious with the increase of $AgInS_2$ amount. These simultaneous shifts in anion and cation ions were probably attributed to the presence of strong electronic interaction between $AgInS_2$ and TiO_2, which were consistent with the previous report [23]. It was speculated that the Ti 2p orbital could lost electrons which could be gained by Ag 3d and In 3d orbitals because of the larger electronegativity of Ag (1.9) and In (1.78) than that of Ti (1.5), leading to the binding energies of the core level electrons increased for Ti 2p and decreased for Ag 3d and In 3d [34,35]. The changes of electrons density in Ti 2p, Ag 3d and In 3d orbitals should have influences on the electrons density of O 1s and S 2p. The XPS results confirmed that the $AgInS_2$ and TiO_2 had been successfully combined.

The XRD patterns of TiO_2, $AgInS_2$ and $AgInS_2/TiO_2$ composites were shown in Fig. 4a. The diffraction peaks of TiO_2 were consistent with TiO_2 (B) phase (JCPDS, No. 46-1238) [36], and the diffraction peaks appeared at 14.2°, 24.9° and 28.6° could be assigned to (001), (110) and (002) crystal planes of TiO_2, respectively. While the peaks of $AgInS_2$ at 26.6°, 28.4°, 43.7° and 44.5° were distinctly indexed to (002), (121), (040), and (320) crystal planes of orthorhombic phase $AgInS_2$ (JCPDS No. 25-1328), respectively. In addition, for all the $AgInS_2/TiO_2$ composites, both TiO_2 and $AgInS_2$ phases could be clearly observed. Moreover, the intensity of diffraction peaks of $AgInS_2$ in composites gradually increased with the increase of $AgInS_2$ concentration. The specific surface area of TiO_2, $AgInS_2$ and $AgInS_2/TiO_2$ were carried out by nitrogen adsorption-desorption technique. As shown in Fig. 4b, the isotherms of all the samples belonged to type III, suggesting their nonporous structures [37], which was in conformity with t-plot result (inset of Fig. 4b). As displayed in Table S1, the S_{BET} of TiO_2 and $AgInS_2$ were 44.48 and 5.04 m^2/g, respectively. The $AgInS_2/TiO_2$ coposites showed decrescent surface area with the increased loading of $AgInS_2$.

In order to reveal the formation of heterojunction between the TiO_2 and $AgInS_2$, zeta potential vs. pH of the aqueous suspensions containing TiO_2 was illustrated in Fig S3. It was found that the point of zero charge (pzc) of the TiO_2 was 3.68, which was closed to the value reported by Zhang [38]. The initial pH of MPA/TiO_2/H_2O system was 3.35 and the TiO_2 surface would remain positively charged in acidic medium (pH < 3.68). According to the acid dissociation constants (pK_{aCOOH} = 4.32) and concentration of MPA, the carboxylic acid (−COOH) of MPA could ionize in water (pH > 2.48) to give hydrogen ion and remain negatively charged [39]. Thus, 3-mercaptopropionic acid would conjugate with TiO_2 by carboxylate radical ($-COO^-$) due to electrostatic attraction. And the terminal thiol group of 3-mercaptopropionic acid could adsorb Ag^+ and In^{3+} to form mercaptide, which

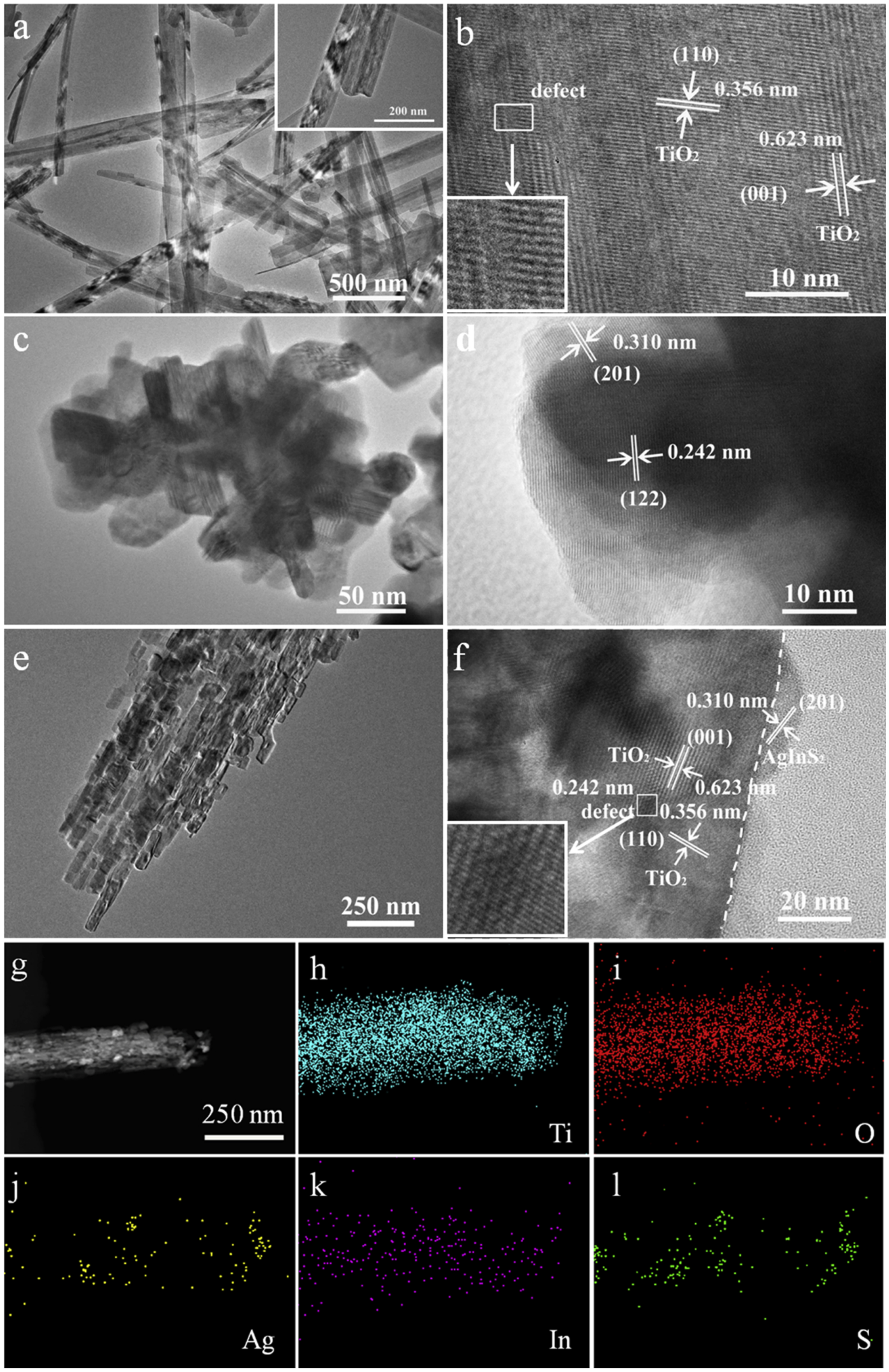

Fig. 2. The TEM (a, c, e) and HRTEM (b, d, f) Images of TiO_2 (a, b), $AgInS_2$ (c, d) and 0.5AT (e, f); TEM image of 0.5AT (g) with a corresponding EDS elemental mapping of Ti (h), O (i), Ag (j), In (k) and S (l).

led to the intimate contact between metallic ions and TiO_2 [40,41]. Finally, thioacetamide was added the mixed solution and acted as a sulfur source to induce the formation of $AgInS_2$ on the surface of TiO_2 under 180 °C for 24 h.

UV-vis DRS of TiO_2, $AgInS_2$ and $AgInS_2/TiO_2$ composites were depicted in Fig. 4c. It was clear that $AgInS_2$ had absorbance both in UV and visible light region, whereas TiO_2 only exhibited absorbance in UV light region. After deposition of $AgInS_2$, the $AgInS_2/TiO_2$ showed obvious absorption in the region of visible light (400–700 nm) compared to TiO_2, and the absorption intensity improved significantly during the UV–vis light range with the increase of $AgInS_2$ loading. The improved solar light harvesting of the hybrid was expected to enhance photocatalytic disinfection for *E. coli*. Moreover, the band gap energies (E_g) of TiO_2 and $AgInS_2$ were calculated using Tauc's plots: $(\alpha h\nu) = A(h\nu - E_g)^{n/2}$, where α, h, ν and A represented the absorption coefficient, Planck's constant, light frequency and constant value, respectively. The E_g of TiO_2, $AgInS_2$ and 0.5AT were estimated to be 3.31, 1.82 and 2.81 eV in this study (Fig. 4d). The detailed calculation process was described in

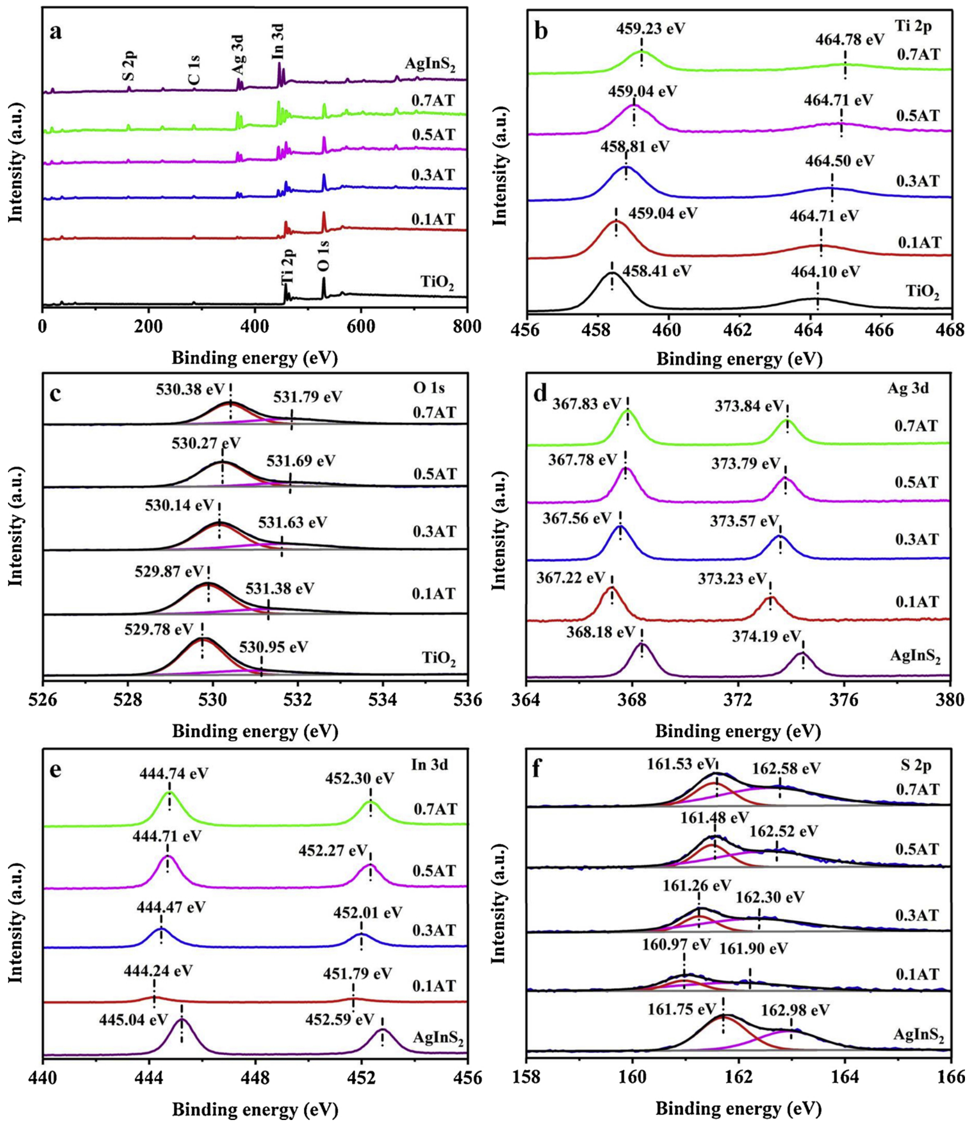

Fig. 3. XPS spectra of TiO_2, $AgInS_2$ and $AgInS_2/TiO_2$ composites: (a) Survey spectrum, (b) Ti 2p, (c) O 1s, (d) Ag 3d, (e) In 3d and (f) S 2p.

Supplementary Material (Fig. S4, S5, Table S2 and S3).

3.2. Photocatalytic disinfection performance

Fig. 5a and b showed the disinfection effect of *E. coli* by catalysts under dark and solar light irradiation with different time intervals (0, 45, 90, 135, and 180 min). As shown in Fig. 5a, the number of *E. coli* decreased from $10^{7.2}$ to $10^{6.0}$ in 45 min and unchanged substantially after 3 h in the dark, indicating that the photocatalyst itself had little bactericidal activity toward the bacteria. In Fig. 5b, when irradiated by light, the bacterial number showed ignorable decrease with time in absence of photocatalyst. With the addition of TiO_2 and $AgInS_2$, the number of bacteria reduced from $10^{7.2}$ to $10^{3.5}$ and $10^{5.2}$ after 180 min of solar light irradiation, respectively. The photocatalytic inactivation efficiency of $AgInS_2/TiO_2$ increased with the increase of $AgInS_2$ in despite of 0.7AT. Particularly, the quantity of viable cells was $10^{2.0}$ and $10^{1.3}$ for 0.1AT and 0.3AT at the end of disinfection, respectively. Notably, the bacterial population were completely inactivated in presence of 0.5AT within 180 min, indicating its superior photocatalytic bactericidal effect. However, with the further increase of $AgInS_2$ loading, the disinfection efficiency of 0.7AT decreased significantly with $10^{4.9}$ of bacteria survived. This result indicated that synergistic effect between TiO_2 and $AgInS_2$ played an important role on the photocatalytic disinfection of the samples. Appropriate amount of $AgInS_2$ has great influence on the light absorption as well as charge transfer in the composites. When the molar ratio of $AgInS_2$ to TiO_2 increased to 0.7:1, a large number of $AgInS_2$ were deposited on the surface of TiO_2. Excess $AgInS_2$ not only occupied the reactive sites of TiO_2 but also acted as new recombination centers, leading to the decreased charge separation and bactericidal effect. Thus, the $AgInS_2$ amount should be control elaborately for increasing the disinfection efficiency of $AgInS_2/TiO_2$. In addition, the photocatalytic disinfection effects of a physical blending of $AgInS_2$ nanosheets and TiO_2 nanobelts ($0.5AgInS_2+TiO_2$) or $AgInS_2$ nanosheets and P25 ($0.5AgInS_2+$P25) were also discussed. Obviously, the disinfection effects of $0.5AgInS_2+TiO_2$ and $0.5AgInS_2+$P25 were much smaller than 0.5AT. This was attributed to the formed heterojunction structures between TiO_2 and $AgInS_2$ in 0.5AT which can accelerate the separation of e^--h^+ pairs.

As the 3D EEM spectra illustrated in Fig. 6a, the initial *E. coli* solution contained two fluorescent peaks: A at Ex/Em of 220 nm/320 nm and B at Ex/Em of 280/300 nm, which was identified as aromatic protein-like and tryptophan protein-like, respectively [31,42]. Those peaks were likely ascribed to the extracellular organic matter secreted by *E. coli*. The increased intensity of peak A and B within 45 min could be considered as the release of cellular organic matters by the decomposition of *E. coli* cells during the photocatalytic process [43]. The peak

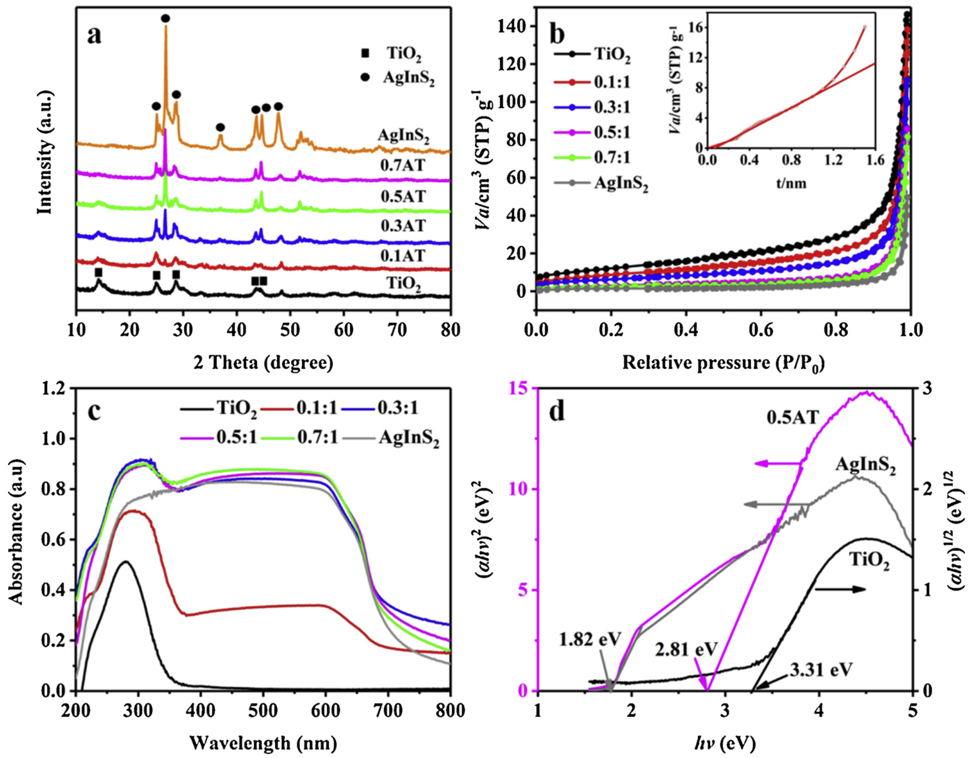

Fig. 4. (a) XRD patterns; (b) N_2 adsorption and desorption isotherms of TiO_2, $AgInS_2$ and $AgInS_2/TiO_2$ composites with different mole ratios (inset: t-Plot of 0.5AT); (c) Diffuse reflectance UV–vis absorption spectra of prepared samples and (d) Estimated band gaps of TiO_2, 0.5AT and $AgInS_2$.

intensities of A and B were decreased with the further extension of time to 135 min. At the end of the experiments, all the peak intensities became weak compared with original bacterial solution, suggesting that *E. coli* cells were inactivated and the released organic matters was degraded by 0.5AT. Therefore, the 3D EEM spectra in conjunction with disinfection effect experiments could confirm the excellent photocatalytic performance of 0.5AT.

3.3. Influences of temperature, humic acid and inorganic anions

To investigate the influence of environmental factors such as temperature, humic acid and inorganic anions, a series of experiments were performed. Temperature was considered as an important factor influencing the activity of bacteria [44]. As shown in Fig. S6a, temperature had great impact on disinfection effect, and the inactivation efficiency increased with the increase of reaction temperature. The complete inactivation of bacterial population was achieved within 180 min for treatment at 25 °C and 35 °C, and only 135 min at 45 °C.

As the major type of natural organic macromolecular, humic acid (HA) widely exists in natural water and is produced by the biodegradation of plant and animal residues. HA have an impact on the transfer, transformation and degradation of organic pollutants because of their wide distribution and strong adsorptive property. It contains abundant functional groups such as hydroxyl, carboxyl, phenolic and so on. In this work, the impacts of HA with different concentrations (0.25, 0.5, 1 and 2 mg/L) on the disinfection efficiency was discussed. As shown in Fig. S6b, the HA had an obvious dose-dependence effect on disinfection efficiency. Remarkably, the disinfection efficiency was enhanced from 45 to 180 min in presence of 0.25 mg/L HA compared to the control treatment. With the HA concentrations were increased from 0.5 to 2 mg/L, the disinfection efficiencies were dramatically decreased, especially for 2 mg/L HA. It has been pointed out that HA can be sensitized by sunlight and transform into triplet excited states (3 DOM*) at low level. 3 DOM* could react with O_2 to form reactive oxygen species (ROS), i.e., $O^{\cdot}H$ and H_2O_2, which could further inactivate *E. coli* [45]. However, the adsorption effect between bacteria and HA would occur because of hydrogen bonds and Vander Waals forces with the increased concentration of HA, which prevented the close contact between bacteria and $AgInS_2/TiO_2$ and thus resulted in low efficiency of the outer membranes decomposition by ROS [46,47]. Moreover, it has been reported that HA could protect *E. coli* against illumination by absorbing sunlight from 270 to 500 nm [48].

The effects of different inorganic anions such as NO_3^-, SO_4^{2-}, HCO_3^- and $H_2PO_4^-$ on the disinfection efficiency of *E. coli* were discussed. As depicted in Fig. S6c, NO_3^- and SO_4^{2-} had obvious inhibiting effect on the bactericidal activity on the preliminary stage of the disinfection process. However, the final efficiencies maintained the same as that of 0.5AT. It was worth noting that HCO_3^- and $H_2PO_4^-$ exerted great depression effect on bacterial inactivation in contrast to NO_3^- and SO_4^{2-}. It was reported that HCO_3^- and $H_2PO_4^-$ could adsorb on the surface of catalysts and capture h^+ during the photocatalytic inactivation process. Furthermore, HCO_3^- and $H_2PO_4^-$ could react with $^{\cdot}OH$ to form $\cdot CO_3^-$ and $^{\cdot}H_2PO_4$ with low oxidative capacities [49].

3.4. Integrity of bacterial cell membranes based on fluorescence microscope and SEM

The fluorescent-based cell live/dead tests of bacterial cells were carried out to confirm inactivation effect of 0.5AT toward *E. coli* (Fig. 7). SYTO9 and PI as the fluorescent nucleic acid dyes were employed to stain the DNA of *E. coli*. SYTO9 stained both live and dead cells with green-fluorescent, whereas PI only stained dead cells with red-fluorescent. There were almost no dead cells in initial *E. coli* solution. Weak red fluorescence appeared after 45 min of illumination with 0.5AT, indicating that cell membranes of *E. coli* were destroyed and labeled by PI. The red fluorescence increased with the extension of irradiation time suggesting that *E. coli* cells were sustainably damaged by reactive species. At the end of exposure, a large number of cells were damaged and cell debris were adsorbed on the surfaces of 0.5AT. However, some green-fluorescent could be seen in 180 min, which was

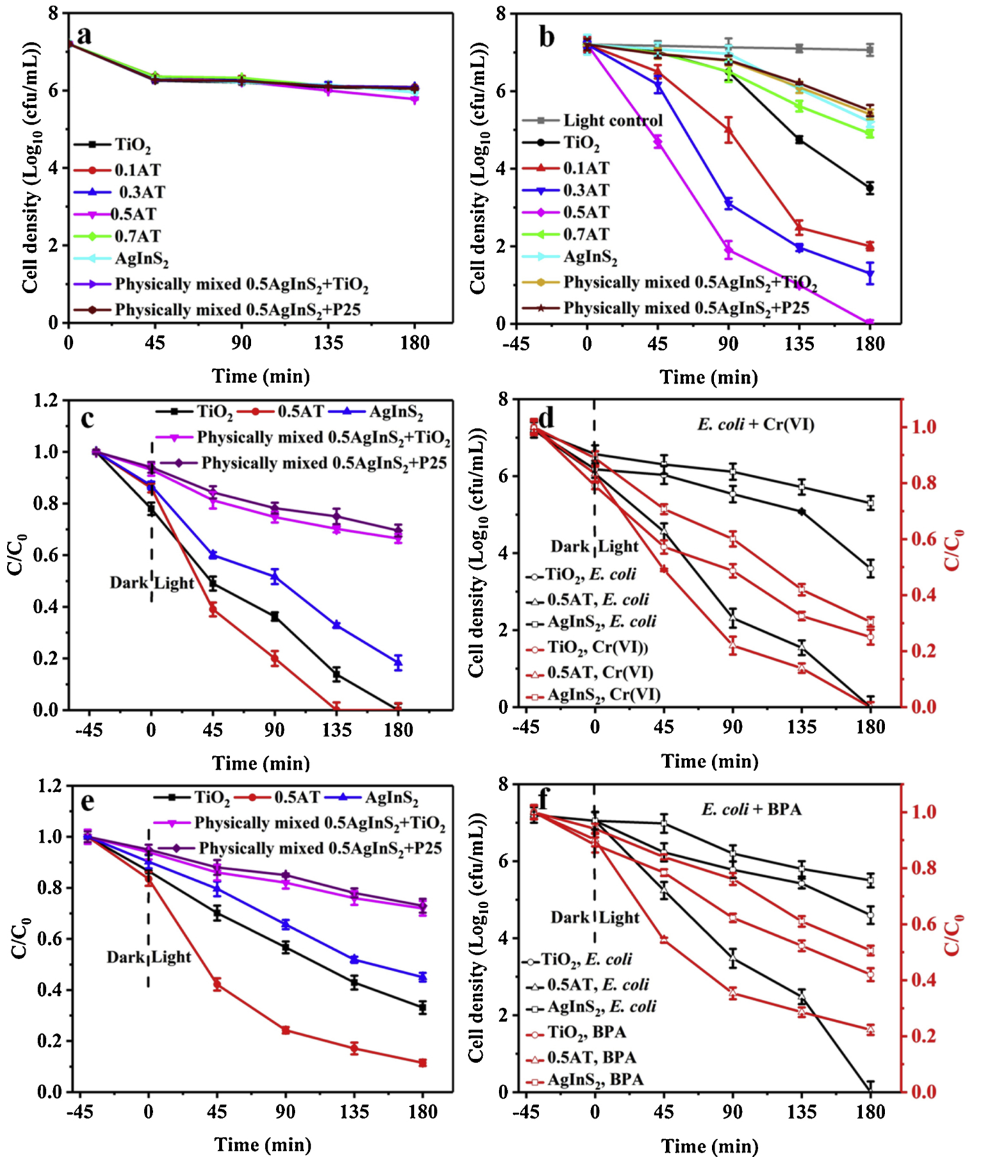

Fig. 5. *E. coli* ($10^{7.2}$ cfu/mL) inactivation by prepared samples in the dark (a) and under solar light irradiation (b); Photocatalytic reduction of Cr(VI) by prepared samples under solar light irradiation (c); Simultaneous *E. coli* inactivation and Cr(VI) reduction under solar light irradiation (d); Photocatalytic degradation of BPA by prepared samples under solar light irradiation (e); Simultaneous *E. coli* inactivation and BPA degradation under solar light irradiation (f).

attribute to some bacteria were not killed by membrane destroy and possibly enter a viable but noncuturable (VBNC) state [50]. Cells in the VBNC state could grow up but fail to divide on the routine bacteriological media. Under these circumstances, no colonies were found by visual inspection after being incubated at 37 °C for 24 h for 0.5AT treatment (Fig. 5b). The bacteria in the VBNC state could be stained by SYTO9 with green-fluorescent but not by PI.

To further study the underlying mechanism during the photocatalytic process, the interaction between bacteria and photocatalyst were imaged using FESEM. According to Fig. S7a, untreated *E. coli* presented a pristine rod shape with intact cell membrane and the length was about 1 μm [51]. It was clear that the cell was undergoing cellular division as indicated by the white arrow in Fig. S7a. Subsequently, after contacted with 0.5AT, the bacteria were adsorbed on the surface of materials and became deformed (Fig. S7b). The surface of cell membrane became wrinkled and the center became roughly sunken, implying that the active species, such as h^+, $^{\cdot}OH$ and $O_2^{\cdot -}$, H_2O_2 were rapidly produced and oxidized the cell membranes in the photocatalytic process [52]. As the irradiation time extended to 45 min, small pits and bulges appeared on the surface (the white ellipse in Fig. S7c), and therefore it was reasonable to speculate that the attacks of different active species should be responsible for these damage phenomena. The shape of the cell was extremely destroyed and the cavities on the surface were enlarged which almost occupied the entire cell surface with the further prolonging illumination (Fig. S7d, e). Reactive species could act on the internal cell contents through the cavities, causing leakage of the internal cell contents [53]. After irradiation for 180 min, the cell was completely distorted. The cell residue combined with 0.5AT was observed, and it was difficult to distinguish the pristine morphology, as indicated by the white arrow in Fig. S7f. Moreover, the morphology changes of *E. coli* after 3 h of treatment for TiO_2, $AgInS_2$ and 0.5AT were also investigated, as shown in Fig. S8. This result further confirmed the best bactericidal effect of 0.5AT than TiO_2 and $AgInS_2$, which was consistent with the inactivation results in Fig. 5b.

3.5. Simultaneous disinfection of E. coliand reduction of Cr(VI)

With the development of electroplating and pigments, Cr(VI) polluted water was generated in a large amount of quantity without effective treatment, which brings about mutagenic and carcinogenic risk

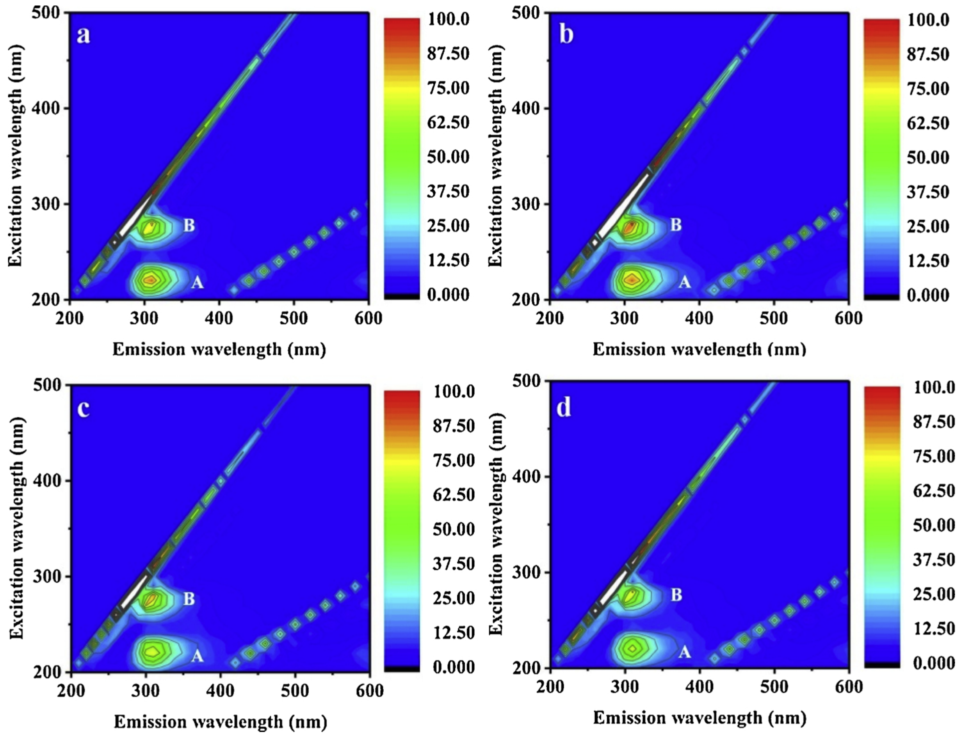

Fig. 6. 3D EEMs of the release and degradation of cellular/extracellular organic maters during the photocatalytic treatment: (a) 0 min, (b) 45 min, (c) 135 min and (d) 180 min.

for human and serious misfunction of ecosystem. In contrast to Cr(VI), the toxicity of Cr(III) is rather less, and thus reducing the Cr(VI) to Cr (III) effectively could reduce the environmental and ecological risk of Cr(VI) [54]. Photocatalytic reduction of Cr (VI) was investigated using TiO_2, $AgInS_2$ and 0.5AT with citric acid as the hole scavenger (1.2 mM). As shown in Fig. 5c, the adsorptive capacity of TiO_2, $AgInS_2$ and 0.5AT toward Cr (VI) within 40 min in the dark was 22.0%, 14.1% and 13.6%, respectively, indicating the best adsorption effect of TiO_2 nanobelts, which could be attributed to its largest specific surface area in Table S1. The Cr (VI) could be reduced completely within 135 min by 0.5AT. After 180 min of solar light irradiation, the reduced efficiency of Cr(VI) over TiO_2 and $AgInS_2$ was 100.0% and 81.7%, respectively. As expected, the photo-reduction activity of 0.5AT was superior to TiO_2 and $AgInS_2$. Meanwhile, the $0.5AgInS_2+TiO_2$ and $0.5AgInS_2$ +P25 were also used for Cr(VI) reduction as reference experiments (Fig. 5c). Obviously, the $0.5AgInS_2$ $+TiO_2$ and $0.5AgInS_2$ +P25 possessed much lower Cr(VI) reductive capacity compared with 0.5AT. The enhanced photoreduction activity of 0.5AT might be attributed to the fact that the matched valence and conduction band positions between TiO_2 and $AgInS_2$ resulted in the formation of heterojunction, which facilitated the harvest of visible light and the separation of electron-hole pairs. Significantly, the coexistence of *E. coli* and Cr(VI) is a pervading problem in water environment, therefore the photocatalytic activity of 0.5AT for the combined pollution of *E. coli* and Cr(VI) was further investigated. In the *E. coli*/Cr(VI)/photocatalyst system, *E. coli* and Cr(VI) acted as scavengers for h^+ and e^-, respectively. As illustrated in Fig. 5d, the adsorption experiment in the dark was carried out for 40 min to achieve an equilibrium adsorption state. The bacterial population were completely inactivated over 0.5AT within 180 min light reaction, and the live bacterial number of TiO_2 and $AgInS_2$ treatments were $10^{3.6}$ and $10^{5.3}$, respectively. At the same time, the reduction efficiency of Cr(VI) was 75.0%, 69.6% and 100.0% for TiO_2, $AgInS_2$ and 0.5AT within 180 min. Therefore, 0.5AT exhibited the best photocatalytic activity in remediation of *E. coli* and Cr(VI) combined pollution compared to TiO_2 and $AgInS_2$.

3.6. Simultaneous disinfection of E. coliand degradation of BPA

BPA as one of the most popular endocrine disruptor compounds, existed widely in water environment [55,56]. The photocatalytic degradation of BPA using TiO_2, $AgInS_2$, 0.5AT, $0.5AgInS_2+TiO_2$ and $0.5AgInS_2$+P25 was investigated. As exhibited in Fig. 5e, 0.5AT showed the highest BPA degradation effect which reached 88.5% within 180 min. Under the same conditions, only 66.8%, 55.0%, 28.0% and 27.1% of BPA was removed by TiO_2, $AgInS_2$, $0.5AgInS_2+TiO_2$ and $0.5AgInS_2$+P25, respectively. In addition, the photocatalytic performance of TiO_2, $AgInS_2$ and 0.5AT was further investigated under the coexistence of BPA and *E. coli*. The BPA itself had very low cytotoxicity against *E. coli* as shown in Fig. S9. From Fig. 5f, it could be observed that *E. coli* cells were completely inactivated by 0.5AT within 180 min, and TiO_2 and $AgInS_2$ showed lower disinfection efficiencies compared with 0.5AT. Meanwhile, 77.71%, 57.98% and 49.39% of BPA was degraded by 0.5AT, TiO_2 and $AgInS_2$, respectively. In conclusion, 0.5AT achieved the best simultaneous *E. coli* disinfection and BPA degradation effect.

3.7. Catalyst stability

To assess the stability of 0.5AT, three cycles of *E. coli* disinfection ($10^{7.2}$ cfu/mL) were implemented under solar light irradiation. After each cycle, the 0.5AT were centrifuged, and then dispersed in 75% of ethanol (10 mL) for ultrasound 5 min. After magnetically stirred for 12 h, the solution was centrifuged and photocatalyst was washed with sterile water several times. Finally, the materials were dried at 60 °C in an oven for next cycle. From Fig. S10a, 0.5AT maintained a high photocatalytic activity after three cycles, indicating its excellent stability. The concentration of Ag^+ was measured by ICP-MS during the recycling experiments. Below 0.08 mg/L of Ag^+ were detected after each cycle. The satisfying recycling results and low Ag^+ leakages were possibly attributed to the alleviative photocorrosion of $AgInS_2$ originating from the stable heterojunction structure between TiO_2 and $AgInS_2$. The XRD, XPS and FESEM of 0.5AT after three cycles were

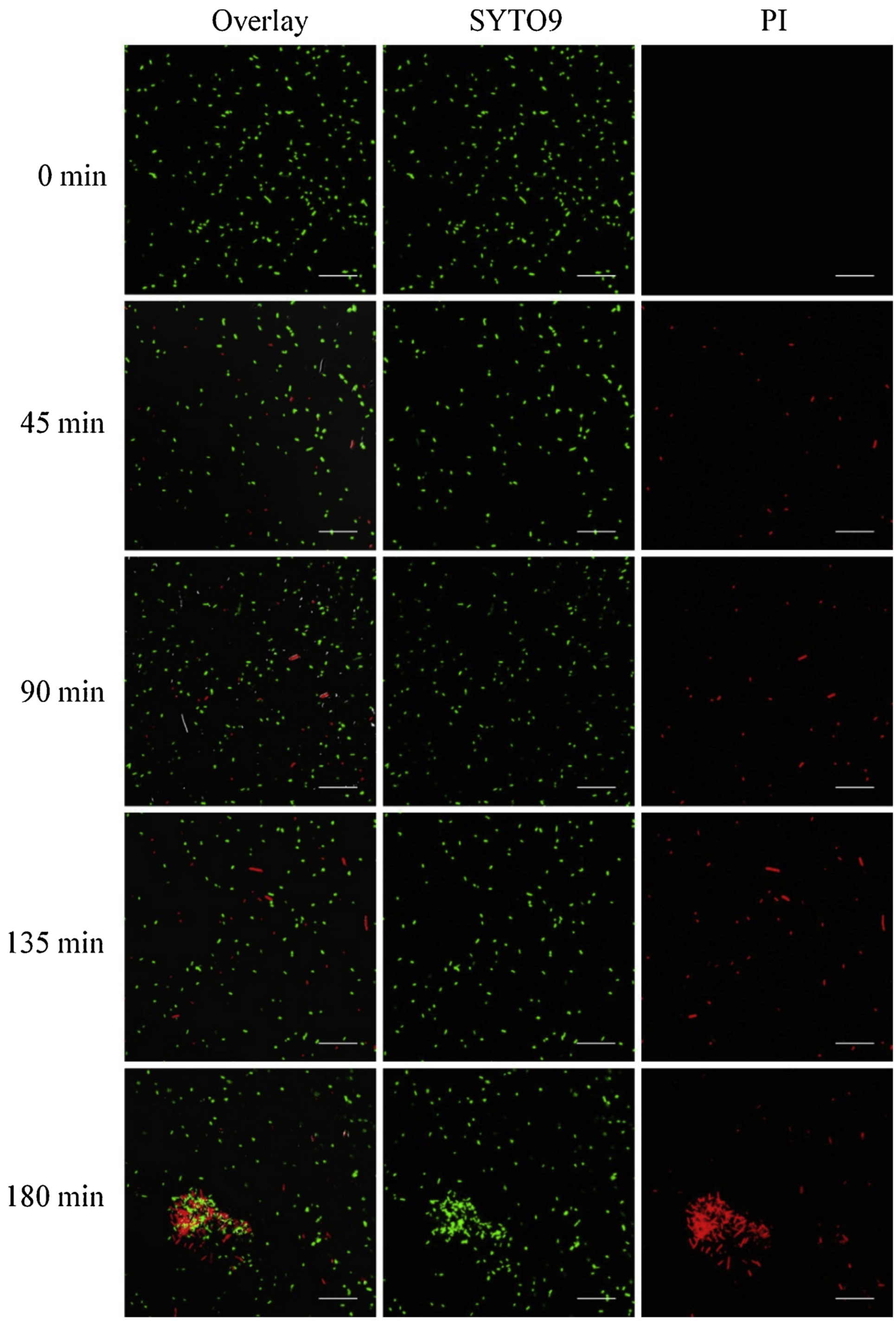

Fig. 7. Fluorescent images of live/dead *E. coli.* The scale bar is 25 µm.

shown in Fig. S10b, S10c and S11. It was clear that no significant change occurred in the crystal pattern and morphology of 0.5AT. The survey XPS spectrum indicated the presence of Ti and O, Ag, In, and S elements in used 0.5AT and the binding energy of the elements were similar to these of fresh one, suggesting the good stability of 0.5AT.

3.8. Photocatalytic mechanisms

To investigate the separation, migration and recombination of photogenerated e^--h^+ pairs in catalysts, photoelectrochemical experiments were carried out. in Fig. 8a. The TiO_2 and $AgInS_2$ showed low photocurrent densities, depicting the quick recombination of photogenerated e^--h^+ pairs. After $AgInS_2$ were deposited on TiO_2, the photocurrent response of $AgInS_2/TiO_2$ increased sharply, implying that the formed heterojunctions could promote e^--h^+ pairs separation in $AgInS_2/TiO_2$. The photocurrents of $AgInS_2/TiO_2$ exhibited good stability and reproducibility in this test, revealing that there were rapid separation and few recombination processes in the heterojunction structure. Furthermore, compared to other catalysts, 0.5AT displayed the highest photocurrent response, demonstrating the fastest e^--h^+ separation rate in the system. These results indicated that the e^--h^+ transferred effectively between $AglnS_2$ and TiO_2, which were beneficial for bacterial inactivation.

Fig. 8b showed the EIS curves under dark for TiO_2, $AgInS_2$ and

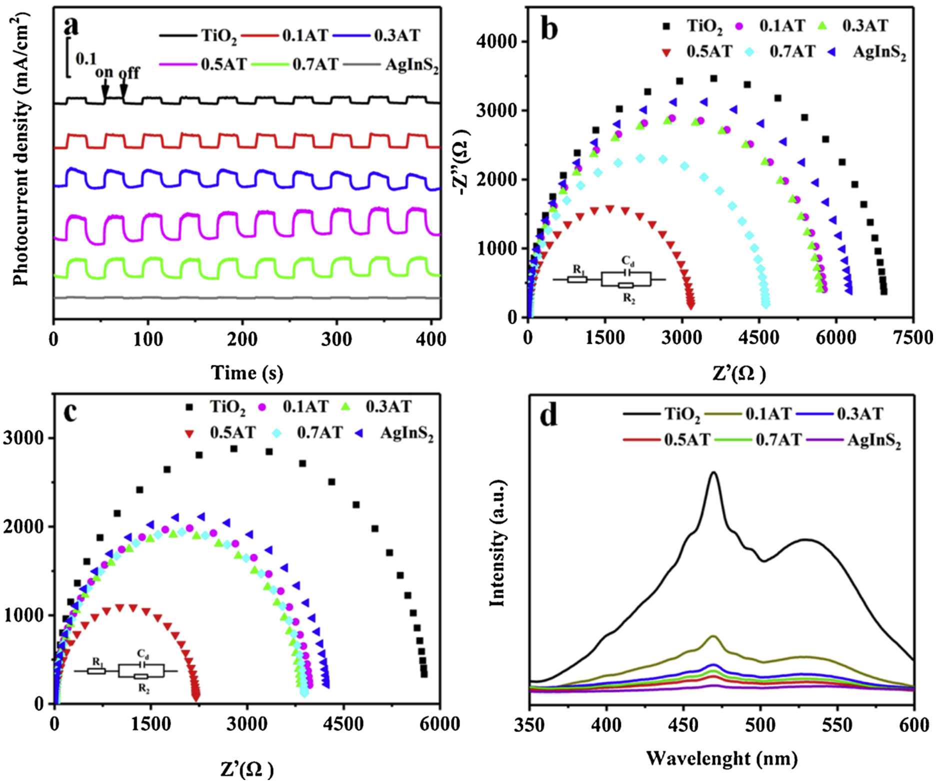

Fig. 8. Photocurrent responses (a), electrochemical impedance spectra under dark (b) and light (c), and PL spectra (d) of the samples.

$AgInS_2/TiO_2$. Generally, a smaller arc size represents a lower impedance, which could manifest a higher separation and transport efficiency of photogenerated e^--h^+ pairs [57]. The arc radius of 0.5AT was the smallest in comparison with other catalysts, suggesting that 0.5AT owned the highest electronic conductivity due to the effective separation and fast interfacial charge transfer of photo-induced carrier. As shown in Fig. 8c, the arc radiuses were decreased under irradiation compared to these in the dark, meaning that the electronic conductivities were increased when the light was on. According to equivalent electrical circuit model, the R_2 represented the charge-transfer resistance from the surface states to the solution (Fig. 8b, c, inset). The larger R_2 value meant the weaker electron transfer rate, which will result in lower photocatalytic disinfection effect [58]. As shown in Table S2, the R_2 value decreased obviously after the formation of heterojunction. Such decrease could imply enhanced transfer efficiency of electron at the electrode/electrolyte interface. Among of all the prepared catalysts, 0.5AT possessed the smallest resistance, which was consistent with its best inactivation effect.

PL spectra were also used to investigate separation efficiency of photogenerated e^--h^+ pairs. Fig. 8d showed the PL spectra of TiO_2, $AgInS_2$ and $AgInS_2/TiO_2$ excited at wavelength of 325 nm. Two strong emission peaks existed at around 469 and 548 nm of TiO_2 were observed. The peak at about 469 nm was assigned to the surface states related to recombination of the electron-hole pairs in TiO_2 [59]. The emission peak at 548 nm was identified to oxygen vacancies on TiO_2 [60]. This result was in good accordance with HRTEM image of TiO_2 which demonstrated the existence of defects. Compared with TiO_2, $AgInS_2/TiO_2$ exhibited similar shapes but depressed PL emissions. $AgInS_2$ could act as a sink for conduction band electrons, promoting efficiently the separation of photogenerated e^--h^+ pairs through the heterojunction interface between TiO_2 and $AgInS_2$ [61]. With the amount of $AgInS_2$ increased, the PL intensity of $AgInS_2/TiO_2$ showed an initial decreasing and then increasing trend, 0.7AT exhibited an enhanced intensity compared with 0.5AT because of the agglomeration of excess $AgInS_2$, which hindered the effective separation of e^--h^+ pairs (Fig. S12). From this, it could be considered that the electron transfer between $AgInS_2$ and TiO_2 was the main reason for promoting photogenerated e^--h^+ pairs separation. Interestingly, the pure $AgInS_2$ displayed weak emission peak, which was consistent with the early report [20]. This phenomenon probably attributed to the failure of aligned orientation between Ag and In led to defects in $AgInS_2$ which was reported by Park et al. and Hamanaka et al. [62,63]. The defects could capture the photogenerated e^- on the CB and reduce the PL quantum efficiencies and fluorescence intensity. Apparently, the results of photocurrent measurements, EIS and PL validated that the fast transfer and separation of charge carriers by a synergistic effect between $AgInS_2$ and TiO_2, thus enhancing the photocatalytic disinfection.

As shown in Fig. 9. Radical trapping agents, such as IPA, sodium oxalate, BQ, Fe(II)-EDTA, Cr(VI) were served as scavengers to $^{\cdot}OH$, h^+, $O^{\cdot}2–$, H_2O_2, and e^-, respectively. When IPA was added into the reaction system, the bactericidal effect showed no significant change compared with no scavenger, suggesting that $O^{\cdot}H$ almost had no contribution to the inactivation process. In addition, the bactericidal effect was obviously inhibited from 45 to 135 min in presence of Fe(II)-EDTA, nevertheless the final cell density was same as that of no scavenger, suggesting that H_2O_2 had a certain contribution to the inactivation of *E. coli*. In the presence of BQ, the cell density significantly decreased, indicating that $O_2^{\cdot}$– played an important role in the photocatalytic system. After adding sodium oxalate, the bacterial inactivation was greatly suppressed, implying that h^+ played a decisive role in the inactivation process. It was obvious that the bactericidal effect was inhibited with addition of Cr(VI), indicating that e^- possibly played an important role in the photocatalytic process. Furthermore, trapping experiment was carried out in the presence of nitrogen and sodium oxalate, under which condition e– was the only reactive species. However, the bactericidal effect was completely depressed with the simultaneous addition of nitrogen and sodium oxalate. This result together with the effect of Cr(VI) manifested that e– mainly react with O_2 to form $O_2^{\cdot}$– during the reaction rather than directly react with *E. coli*. To further confirm the major contribution of active species, TA, NBT, $TiOSO_4$ were used as the

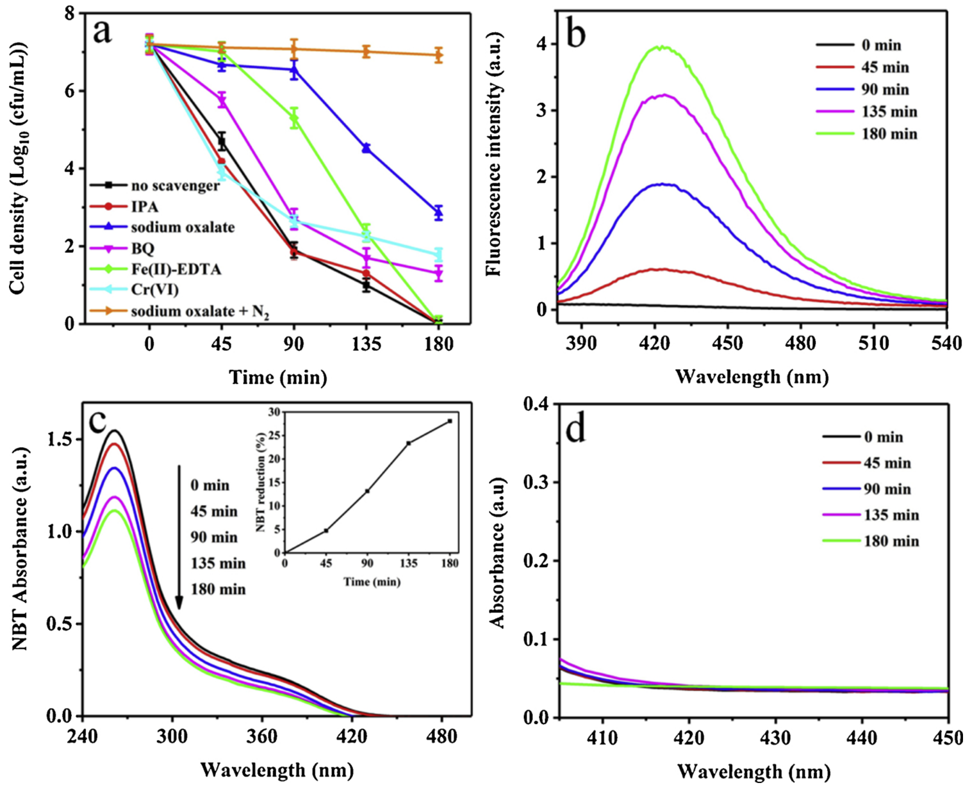

Fig. 9. (a) Photocatalytic inactivation efficiencies against *E. coli* ($10^{7.2}$ cfu/mL) with different scavengers; (b) the fluorescence spectra of TAOH; (c) the UV absorption spectra of NBT; (d) hydrogen peroxide detection using $TiOSO_4$.

specified probe for ˙OH, O˙2⁻and H_2O_2, respectively. As shown in Fig. 9b, the fluorescent signal of TAOH at 425 nm increased with irradiation time from 0 min to 180 min, indicating the O˙H were generated from 0.5AT under solar light illumination [25]. However, the signal of O˙H was weak compared to other reports [25,64], which was due to the few quantity and short half-life time of O˙H. The concentrations of NBT

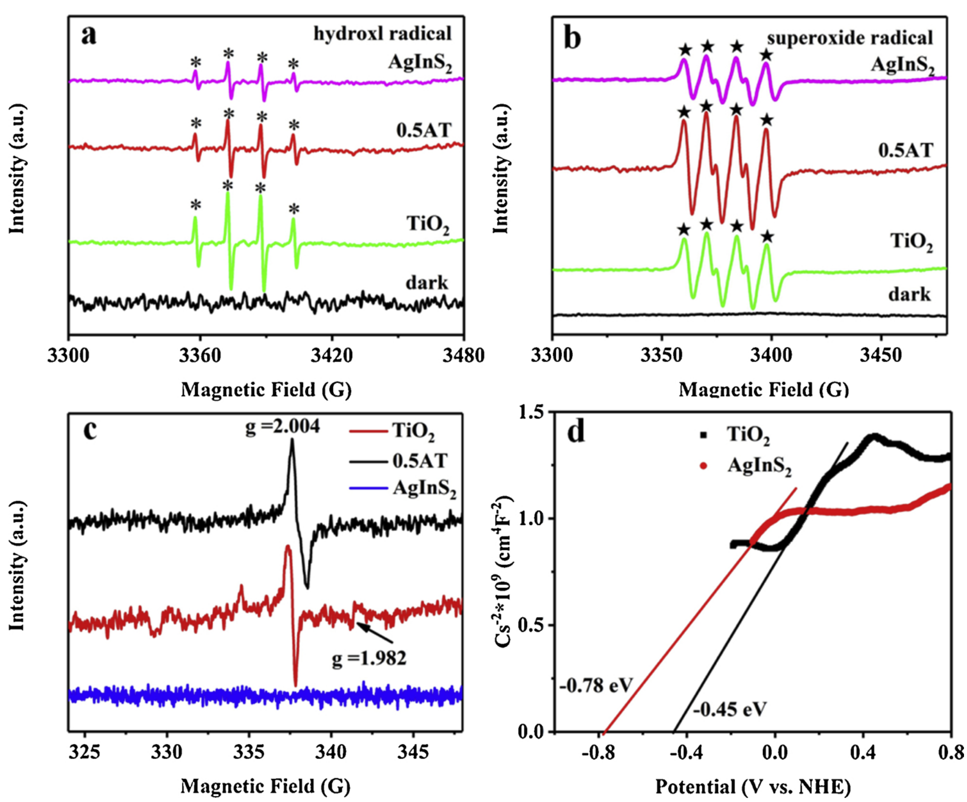

Fig. 10. (a, b) EPR spectra of DMPO-˙OH, DMPO-$O_2^{\cdot-}$; (c) EPR spectra of TiO_2, 0.5AT and $AgInS_2$; (d) Mott-Schottky plots for TiO_2 and $AgInS_2$.

at 259 nm had changed over time (Fig. 9c), and transformation percentage of NBT was 28.1% (inset of Fig. 9c) at 180 min, implying that a certain amount of $O_2^{\cdot-}$ radicals generated from 0.5AT heterostructure. Nevertheless, the difference of generated H_2O_2 at different times could be ignored (Fig. 9d), which further confirmed the unnecessary role of H_2O_2.

The reactive species of $^{\cdot}OH$ and $O_2^{\cdot-}$ were also detected by EPR measurements. As depicted in Fig. 10 a and b, no characteristic signals could be observed in dark for both DMPO-$^{\cdot}OH$ and DMPO-$O_2^{\cdot-}$. According to the early report, the production of $^{\cdot}OH$ and $O_2^{\cdot-}$ production affected by excitation wavelength and illumination time [65,66]. Therefore, the signals of DMPO-$O^{\cdot}H$ (1:2:2:1) and DMPO-$O_2^{\cdot-}$ (1:1:1:1) of different catalysts was detected at same irradiation time of 10 min and same light source. $^{\cdot}OH$ and $O_2^{\cdot-}$ radicals were all be found in these photocatalytic systems. According to Fig. 5, the 0.5AT exhibited superior photocatalytic activity, which was consistent with the strong signal of $O_2^{\cdot-}$ (Fig. 10b). However, the 0.5AT exhibited the intermediate signal of $O^{\cdot}H$ compared with TiO_2 and $AgInS_2$ (Fig. 10a). This was because $O^{\cdot}H$ had no contribution in the photocatalytic system. The production of $^{\cdot}OH$ and $O_2^{\cdot-}$ were related to the conduction band position (E_{CB}) and valence band potential (E_{VB}) of catalyst, which were described in photocatalytic mechanism. Additionally, the oxygen vacancies of TiO_2, 0.5AT and $AgInS_2$ were also studied by EPR analysis without light illumination (Fig. 10c). However, no signals were observed for the $AgInS_2$. The symmetrical paramagnetic signals appeared approximately at g = 2.004 both in TiO_2 nanobelt and 0.5AT. It was reported that the signal at g = 2.004 was attributed to the trapped electron on the oxygen vacancy [32]. Therefore, it indicated that the oxygen vacancies existed in TiO_2 nanobelt and 0.5AT, which further confirmed the results of HRTEM and PL. The electrons could be captured by oxygen vacancies and react with O_2 to produce reactive oxygen species [67], which had contribution to the photocatalytic disinfection effect. Simultaneously, a week signal at g = 1.982 was found on pure TiO_2, which was attributed to Ti^{3+} species [68]. However, the signal at g = 1.982 could not be found on 0.5AT, possibly ascribing to the much low concentration of Ti^{3+} defects in 0.5AT.

Mott-Schottky plots were employed to investigate the flat band potential of TiO_2 and $AgInS_2$ (Fig. 10d). Obviously, TiO_2 and $AgInS_2$ were n-type semiconductors because of the positive slopes of their Mott-Schottky plots [37]. The flat potentials of TiO_2 and $AgInS_2$ were approximately -0.45 and -0.78 eV versus normal hydrogen electrode (NHE), respectively. As far as we know, the Fermi levels (E_f) of n-type semiconductor was adjacent to the flat-band potential and 0.2 eV lower than the E_{CB} [69]. Therefore, the E_f of TiO_2 and $AgInS_2$ could be considered to be -0.45 and -0.78 eV (vs. NHE), and the E_{CB} of TiO_2 and $AgInS_2$ could be estimated to be -0.65 and -0.98 eV, respectively. According to their band gaps in Fig. 4d, the E_{VB} of TiO_2 and $AgInS_2$ could be estimated to be +2.66 and +0.84 eV, respectively.

A tentative mechanism of photocatalytic disinfection of *E. coli* and reduction of Cr(VI) over type II heterojunction between TiO_2 and $AgInS_2$ was proposed on the basis of the above results (Fig. 11). Under solar light irradiation, e^- could be excited from the VB of TiO_2 and $AgInS_2$ to their corresponding CB and left h^+ on VB. The photogenerated e^-on the CB of $AgInS_2$ (-0.98 eV) could quickly migrate to the CB of TiO_2 (-0.65 eV). Meanwhile, the h^+ on the VB of TiO_2 (+2.66 eV) could transfer easily to the VB of $AgInS_2$ (+0.84 eV). Therefore, the photogenerated carriers within the $AgInS_2/TiO_2$ could be successfully separated. Moreover, the appropriate amount of oxygen vacancies in this system could also capture electrons and inhibit the recombination of free e^- and h^+. In the process of photocatalysis, the e^- on TiO_2 could directly reduce Cr(VI) to Cr(III). Simultaneously, $O_2^{\cdot-}$ was generated by the reduction of O_2 because the CB of TiO_2 was more negative than the potential of $O_2/O_2^{\cdot-}$ (-0.046 eV vs. NHE), which was approved by radical trapping experiments, detection of NBT concentration experiment and ESR technique. The h^+ remained at the VB of $AgInS_2$ (+0.84 eV vs. NHE) could not oxidize OH^-or H_2O to $O^{\cdot}H$ due to its lower potential than $OH^-/O^{\cdot}H$ (+2.34 eV) or $H_2O/O^{\cdot}H$ (+1.99 eV) [70], which was consistent with the results of scavengers and EPR. As shown in Fig. 10a, the intensity of $O^{\cdot}H$ could be arranged in the following order as: $AgInS_2$ < 0.5AT < TiO_2. The strong signal of $O^{\cdot}H$ over TiO_2 could be explained by the direct reaction of h^+ on the VB of TiO_2 with OH^- or H_2O. Although the h^+ on the VB of $AgInS_2$ (+0.84 eV) could not directly oxidize OH^- or H_2O to $O^{\cdot}H$, a little amount of $O^{\cdot}H$ radicals over $AgInS_2$ were still detected. This $O^{\cdot}H$ signals possibly ascribed to final product for reduction effect of O_2 by e^-. Compared to $AgInS_2$, 0.5AT had a stronger signal of $O^{\cdot}H$, which was attributed to the formed heterojunction between TiO_2 and $AgInS_2$ benefiting the faster separation of photogenerated e^--h^+ and thereby more productive free electrons. As shown in Fig. 10b, the 0.5AT obtained the most abundant $O_2^{\cdot-}$, following was TiO_2, and the least was $AgInS_2$. However, the $AgInS_2$ should have the maximum $O_2^{\cdot-}$ quantity according to its most negative conduct band position. This contradiction possibly owned to the rapid recombination of e^- and h^+ in $AgInS_2$. The most quantity of produed $O_2^{\cdot-}$ by 0.5AT could be ascribed to the formation of type II heterojunction between TiO_2 and $AgInS_2$ with matched valence and conduction position, which was beneficial to the highly efficient separation and reduced recombination of e^- and h^+. Moreover, the appropriate amount of oxygen vacancies could introduce mid-gap states, which located blew the CB of 0.75–1.18 eV to capture electrons and inhibit the recombination of free electron and hole, thereby enhancing the photocatalytic activity [32,67]. Therefore, the abundant h^+ and $O_2^{\cdot-}$ produced over $AgInS_2/TiO_2$ with high oxidative capacities could degrade BPA and disinfect *E. coli*. Simultaneously, the produced e^- was the predominant active species for reducing Cr(VI) to Cr(III) [71].

4. Conclusions

In this study, the efficient photocatalyst $AgInS_2/TiO_2$ have been synthesized by simple hydrothermal process. The obtained 0.5AT composite exhibited much enhanced photocatalytic activities for inactivated bacteria, degraded BPA, or reduced Cr(VI). The bacterial population of $10^{7.2}$ was completely inactivated within 180 min, 88.5% of BPA was degraded within 180 min and 100.0% of Cr(VI) was reduced within 135 min in the presence of 0.5AT under solar light irradiation. Moreover, the effective simultaneous removal of bacteria and Cr(VI) or bacteria and BPA over 0.5AT were achieved. The improved photocatalytic disinfection efficiency, Cr(VI) reduction and BPA degradation could be attributed to the enhanced light harvesting and effective photogenerated e– and h^+ separation through the construction of heterojunction between TiO_2 and $AgInS_2$. The oxygen vacancies also could be detected in TiO_2 and $AgInS_2/TiO_2$, which was conducive to the photocatalytic process. Simultaneously, the excellent recycling effect and low leaking Ag^+ were achieved which possibly ascribed to the alleviative $AgInS_2$ photocorrosion resulting from the stable heterojunction structure between TiO_2 and $AgInS_2$. In a word, this work provides a new strategy to design novel 2D/1D photocatalysts with enhanced photocatalytic remediation effect towards combined pollution of pathogenic bacteria and heavy metal ion or pathogenic bacteria and emerging organic pollutant.

Declaration of Competing Interest

The authors declare that they have no known competing financial interests or personal relationships that could have appeared to influence the work reported in this paper.

Acknowledgements

This work is supported by the Science and Technology Innovation Talents Program of Xinxiang City, China (CXRC17001), Major Science and Technology Program for Water Pollution Control and Treatment of

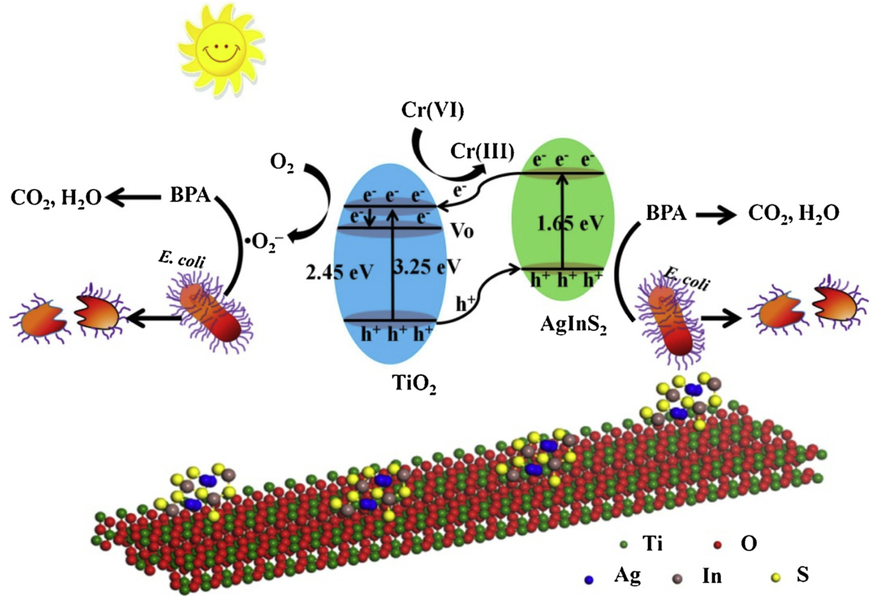

Fig. 11. Proposed schematic diagram of photocatalytic disinfection for *E. coli,* Cr(VI) reduction and BPA degradation under solar light over $AgInS_2/TiO_2$ composite.

China (2015ZX07204-002), Foundation of Henan Normal University (20180446), the special fund for topnotch talents in Henan Agricultural University (30500600) and the Project Plan of Key Scientific Research in Colleges and Universities of Henan Province (16A150060, 19A610001).

Appendix A. Supplementary data

Supplementary material related to this article can be found, in the online version, at doi:https://doi.org/10.1016/j.apcatb.2019.118062.

References

[1] X. Zeng, D.T. McCarthy, A. Deletic, X. Zhang, Silver/reduced graphene oxide hydrogel as novel bactericidal filter for point-of-use water disinfection, Adv. Funct. Mater. 25 (2015) 4344–4351, https://doi.org/10.1002/adfm.201501454.
[2] D. Xia, H. Liu, B. Xu, Y. Wang, Y. Liao, Y. Huang, L. Ye, C. He, P.K. Wong, R. Qiu, Single Ag atom engineered 3D-MnO_2 porous hollow microspheres for rapid photothermocatalytic inactivation of *E. coli* under solar light, Appl. Catal. B 245 (2019) 177–189, https://doi.org/10.1016/j.apcatb.2018.12.056.
[3] Q. Zhou, S. Ma, S. Zhan, Superior photocatalytic disinfection effect of Ag-3D ordered mesoporous CeO_2 under visible light, Appl. Catal. B 224 (2018) 27–37, https://doi.org/10.1016/j.apcatb.2017.10.032.
[4] G.Q. Li, Z. Huo, Q. Wu, Y. Lu, H. Hu, Synergistic effect of combined UV-LED and chlorine treatment on *Bacillus subtilis spore* inactivation, Sci. Total Environ. 639 (2018) 1233–1240, https://doi.org/10.1016/j.scitotenv.2018.05.240.
[5] O.M. Lee, H.Y. Kim, W. Park, T.H. Kim, S. Yu, A comparative study of disinfection efficiency and regrowth control of microorganism in secondary wastewater effluent using UV, ozone, and ionizing irradiation process, J. Hazard. Mater. 295 (2015) 201–208, https://doi.org/10.1016/j.jhazmat.2015.04.016.
[6] M.R. Shariati, A. Samadi-Maybodi, A.H. Colagar, Exploration of charge carrier delocalization in the iron oxide/CdS type-II heterojunction band alignment for enhanced solar-driven photocatalytic and antibacterial applications, J. Hazard. Mater. 366 (2019) 475–481, https://doi.org/10.1016/j.jhazmat.2018.12.025.
[7] T. Matsunaga, R. Tomoda, T. Nakajima, H. Wake, Photoelectrochemical sterilization of microbial cells by semiconductor powders, FEMS Microbiol. Lett. 29 (1985) 211–214, https://doi.org/10.1111/j.1574-6968.1985.tb00864.x.
[8] G. Yang, H. Yin, W. Liu, Y. Yang, Q. Zou, L. Luo, H. Li, Y. Huo, H. Li, Synergistic Ag/TiO_2-N photocatalytic system and its enhanced antibacterial activity towards *Acinetobacter baumannii*, Appl. Catal. B 224 (2018) 175–182, https://doi.org/10.1016/j.apcatb.2017.10.052.
[9] Q. Chen, S. Wu, Y. Xin, Synthesis of Au-CuS-TiO_2 nanobelts photocatalyst for efficient photocatalytic degradation of antibiotic oxytetracycline, Chem. Eng. J. 302 (2016) 377–387, https://doi.org/10.1016/j.cej.2016.05.076.
[10] B. Liu, Y. Xue, J. Zhang, B. Han, J. Zhang, X. Suo, L. Mu, H. Shi, Visible-light-driven TiO_2/Ag_3PO_4 heterostructures with enhanced antifungal activity against agricultural pathogenic *fungi Fusarium graminearum* and mechanism insight, Environ. Sci. Nano 4 (2017) 255–264, https://doi.org/10.1039/C6EN00415F.
[11] S.G. Kim, L.K. Dhandole, Y.S. Seo, H.S. Chung, W.S. Chae, M. Cho, J.S. Jang, Active composite photocatalyst synthesized from inactive Rh & Sb doped TiO_2 nanorods: enhanced degradation of organic pollutants & antibacterial activity under visible light irradiation, Appl. Catal. A Gen. 564 (2018) 43–55, https://doi.org/10.1016/j.apcata.2018.07.016.
[12] J. Wang, M. Li, M. Zhi, A. Manivannan, N. Wu, Hydrothermal synthesis and photocatalytic activity of titanium dioxide nanotubes, nanowires and nanospheres, Mater. Res. Soc. Symp. Proc. 1144 (2009), https://doi.org/10.1557/PROC-1144-LL07-08 LL07-08.
[13] J. Wang, W. Liu, H. Li, H. Wang, Z. Wang, W. Zhou, H. Liu, Preparation of cellulose fiber-TiO_2 nanobelt-silver nanoparticle hierarchically structured hybrid paper and its photocatalytic and antibacterial properties, Chem. Eng. J. 228 (2013) 272–280, https://doi.org/10.1016/j.cej.2013.04.098.
[14] J. Shim, Y.S. Seo, B.T. Oh, M. Cho, Microbial inactivation kinetics and mechanisms of carbon-doped TiO_2 (C-TiO_2) under visible light, J. Hazard. Mater. 306 (2016) 133–139, https://doi.org/10.1016/j.jhazmat.2015.12.013.
[15] P. Ribao, J. Corredor, M.J. Rivero, I. Ortiz, Role of reactive oxygen species on the activity of noble metal-doped TiO_2 photocatalysts, J. Hazard. Mater. 372 (2019) 45–51, https://doi.org/10.1016/j.jhazmat.2018.05.026.
[16] E. Kusiak-Nejman, A.W. Morawski, TiO_2/graphene-based nanocomposites for water treatment: a brief overview of charge carrier transfer, antimicrobial and photocatalytic performance, Appl. Catal. B 253 (2019) 179–186, https://doi.org/10.1016/j.apcatb.2019.04.055.
[17] D. Jiang, J. Xue, L. Wu, W. Zhou, Y. Zhang, X. Li, Photocatalytic performance enhancement of CuO/Cu_2O heterostructures for photodegradation of organic dyes: effects of CuO morphology, Appl. Catal. B 211 (2017) 199–204, https://doi.org/10.1016/j.apcatb.2017.04.034.
[18] M. Sun, Z. Chen, J. Li, J. Hou, F. Xu, L. Xu, R. Zeng, Enhanced visible light-driven activity of TiO_2 nanotube array photoanode co-sensitized by “green” $AgInS_2$ photosensitizer and In_2S_3 buffer layer, Electrochim. Acta 269 (2018) 429–440, https://doi.org/10.1016/j.electacta.2018.03.035.
[19] J. Liu, S. Chen, Q. Liu, Y. Zhu, Y. Lu, Density functional theory study on electronic and photocatalytic properties of orthorhombic $AgInS_2$, Comput. Mater. Sci. 91 (2014) 159–164, https://doi.org/10.1016/j.commatsci.2014.05.010.
[20] B. Liu, X. Li, Q. Zhao, J. Ke, M. Tadé, S. Liu, Preparation of $AgInS_2/TiO_2$ composites for enhanced photocatalytic degradation of gaseous o-dichlorobenzene under visible light, Appl. Catal. B 185 (2016) 1–10, https://doi.org/10.1016/j.apcatb.2015.12.003.
[21] M. Zhang, X. Li, Q. Zhao, S. Fan, Z. Jiang, G. Chen, $AgInS_2$ nanoparticles modified TiO_2 nanotube array electrodes: ultrasonic-assisted SILAR preparation and mechanism of enhanced photoelectrocatalytic activity, Mol. Catal. 442 (2017) 97–106, https://doi.org/10.1016/j.mcat.2017.09.009.
[22] X. Cui, H. Gu, Y. Guan, G. Ren, Z. Ma, Y. Yin, J. Liu, X. Cui, L. Yao, Y. Yin, D. Wang, G. Jin, S. Rong, L. Tong, J. Hou, M. Li, Fabrication of $AgInS_2$ nanoparticles sensitized TiO_2 nanotube arrays and their photoelectrochemical properties, Energy Mater. Sol. Cells 137 (2015) 101–106, https://doi.org/10.1016/j.solmat.2015.01.036.
[23] G. Yang, D. Chen, H. Ding, J. Feng, J. Zhang, Y. Zhu, S. Hamid, D.W. Bahnemann, Well-designed 3D $ZnIn_2S$ nanosheets/TiO_2 nanobelts as direct Z- scheme photocatalysts for CO_2 photoreduction into renewable hydrocarbon fuel with high efficiency, Appl. Catal. B 219 (2017) 611–618, https://doi.org/10.1016/j.apcatb.2017.08.016.
[24] M.V. Dozzi, S. Marzorati, M. Longhi, M. Coduri, L. Artiglia, E. Selli, Photocatalytic activity of TiO_2-WO_3 mixed oxides in relation to electron transfer efficiency, Appl. Catal. B 186 (2016) 157–165, https://doi.org/10.1016/j.apcatb.2016.01.004.
[25] F. Xu, J. Zhang, B. Zhu, J. Yu, J. Xu, $CuInS_2$ sensitized TiO_2 hybrid nanofibers for improved photocatalytic CO_2 reduction, Appl. Catal. B 230 (2018) 194–202, https://doi.org/10.1016/j.apcatb.2018.02.042.
[26] H. Shi, Y. Zhao, J. Fan, Z. Tang, Construction of novel Z-scheme flower-like Bi_2S_3/$SnIn_4S_8$ heterojunctions with enhanced visible light photodegradation and bactericidal activity, Appl. Surf. Sci. 465 (2019) 212–222, https://doi.org/10.1016/j.

apsusc.2018.09.164.
[27] D. Xia, H. Liu, Z. Jiang, T.W. Ng, W.S. Lai, T. An, W. Wang, P.K. Wong, Visible-light-driven photocatalytic inactivation of *Escherichia coli* K-12 over thermal treated natural magnetic sphalerite: band structure analysis and toxicity evaluation, Appl. Catal. B 224 (2018) 541–552, https://doi.org/10.1016/j.apcatb.2017.10.030.
[28] L. Zeng, W. Song, M. Li, D. Zeng, C. Xie, Catalytic oxidation of formaldehyde on surface of $HTiO_2$/$HCTiO_2$ without light illumination at room temperature, Appl. Catal. B 147 (2014) 490–498, https://doi.org/10.1016/j.apcatb.2013.09.013.
[29] K. Qi, S. Liu, M. Qiu, Photocatalytic performance of TiO_2 nanocrystals with/without oxygen defects, Chin. J. Catal. 39 (2018) 867–875, https://doi.org/10.1016/S1872-2067(17)62999-1.
[30] Y. Xu, W. Wen, J.M. Wu, Titania nanowires functionalized polyester fabrics with enhanced photocatalytic and antibacterial performances, J. Hazard. Mater. 343 (2018) 285–297.
[31] C. Su, W. Li, Y. Lu, M. Chen, Z. Huang, Effect of heterogeneous Fenton-like pretreatment on anaerobic granular sludge performance and microbial community for the treatment of traditional Chinese medicine wastewater, J. Hazard. Mater. 314 (2016) 51–58, https://doi.org/10.1016/j.jhazmat.2016.04.024.
[32] N. Shi, X. Li, T. Fan, H. Zhou, J. Ding, D. Zhang, H. Zhu, Biogenic N-I-codoped TiO_2 photocatalyst derived from kelp for efficient dye degradation, Energy Environ. Sci. 4 (2011) 172–180.
[33] Y. Sheng, Z. Wei, H. Miao, W. Yao, H. Li, Y. Zhu, Enhanced organic pollutant photodegradation via adsorption/photocatalysis synergy using a 3D g-C_3N_4/TiO_2 free-separation photocatalyst, Chem. Eng. J. 370 (2019) 287–294, https://doi.org/10.1016/j.cej.2019.03.197.
[34] Q. Li, Y. Xia, C. Yang, K. Lv, M. Lei, M. Li, Building a direct Z-scheme heterojunction photocatalyst by $ZnIn_2S_4$ nanosheets and TiO_2 hollowspheres for highly-efficient artificial photosynthesis, Chem. Eng. J. 349 (2018) 287–296, https://doi.org/10.1016/j.cej.2018.05.094.
[35] L. Yuan, C. Han, M. Pagliaro, Y.J. Xu, Origin of enhancing the photocatalytic performance of TiO_2 for artificial photoreduction of CO_2 through a SiO_2 coating strategy, J. Phys. Chem. C 120 (2016) 265–273, https://doi.org/10.1021/acs.jpcc.5b08893.
[36] Z. Wang, Y. Wang, W. Zhang, Z. Wang, Y. Ma, X. Zhou, Fabrication of TiO_2(B)/anatase heterophase junctions at high temperature via stabilizing the surface of TiO_2(B) for enhanced photocatalytic activity, J. Phys. Chem. C 123 (2019) 1779–1789, https://doi.org/10.1021/acs.jpcc.8b09763.
[37] T. Wang, M. Sun, H. Sun, J. Shang, P.K. Wong, Efficient Z-scheme visible-light-driven photocatalytic bacterial inactivation by hierarchical MoS_2-encapsulated hydrothermal carbonation carbon core-shell nanospheres, Appl. Surf. Sci. 464 (2019) 43–52, https://doi.org/10.1016/j.apsusc.2018.09.060.
[38] L. Zhang, H. Bai, L. Liu, D. Sun, Dimension induced intrinsic physio-electrical effects of nanostructured TiO_2 on its antibacterial properties, Chem. Eng. J. 334 (2018) 1309–1315, https://doi.org/10.1016/j.cej.2017.11.075.
[39] H. Zhang, Z. Zhou, B. Yang, M. Gao, The Influence of carboxyl groups on the photoluminescence of mercaptocarboxylic acid-stabilized CdTe nanoparticles, J. Phys. Chem. B 107 (2003) 8–13, https://doi.org/10.1021/jp025910c.
[40] Y. Chen, S. Hu, W. Liu, X. Chen, L. Wu, X. Wang, P. Liu, Z. Li, Controlled syntheses of cubic and hexagonal $ZnIn_2S_4$ nanostructures with different visible-light photocatalytic performance, Dalton Trans. 40 (2011) 2607–2613, https://doi.org/10.1039/c0dt01435d.
[41] J. Qin, X. Hu, X. Li, Z. Yin, B. Liu, Kh. Lam, 0D/2D $AgInS_2$/MXene Z-scheme heterojunction nanosheets for improved ammonia photosynthesis of N_2, Nano Energy 61 (2019) 27–35, https://doi.org/10.1016/j.nanoen.2019.04.028.
[42] L. Pang, J. Ni, X. Tang, Fast characterization of soluble organic intermediates and integrity of microbial cells in the process of alkaline anaerobic fermentation of waste activated sludge, Biochem. Eng. J. 86 (2014) 49–56, https://doi.org/10.1016/j.bej.2014.03.005.
[43] J. Song, X. Wang, J. Ma, X. Wang, J. Wang, J. Zhao, Visible-light-driven in situ inactivation of *Microcystis aeruginosa* with the use of floating g-C_3N_4 heterojunction photocatalyst: performance, mechanisms and implications, Appl. Catal. B 226 (2018) 83–92, https://doi.org/10.1016/j.apcatb.2017.12.034.
[44] S. Ma, S. Zhan, Y. Jia, Q. Zhou, Highly efficient antibacterial and Pb(II) removal effects of Ag-$CoFe_2O_4$-GO nanocomposite, ACS Appl. Mater. Interfaces 7 (2015) 10576–10586, https://doi.org/10.1021/acsami.5b02209.
[45] Y. Lester, C.M. Sharpless, H. Mamane, K.G. Linden, Production of photo oxidants by dissolved organic matter during UV water treatment, Environ. Sci. Technol. 47 (2013) 11726–11733, https://doi.org/10.1021/es402879x.
[46] S. Ma, S. Zhan, Y. Jia, Q. Shi, Q. Zhou, Enhanced disinfection application of Ag-modified g-C_3N_4 composite under visible light, Appl. Catal. B 186 (2016) 77–87, https://doi.org/10.1016/j.apcatb.2015.12.051.
[47] C. Deng, J. Gong, G. Zeng, Y. Jiang, C. Zhang, H. Liu, S. Huan, Graphene-CdS nanocomposite inactivation performance toward *Escherichia coli* in the presence of humic acid under visible light irradiation, Chem. Eng. J. 284 (2016) 41–53, https://doi.org/10.1016/j.cej.2015.08.106.
[48] A. Muela, J.M. García-Bringas, I. Arana, I. Barcina, Humic materials offer photoprotective effect to *Escherichia coli* exposed to damaging luminous radiation, Microb. Ecol. 40 (2000) 336–344, https://doi.org/10.1007/s002480000064.
[49] A. Rincon, Effect of pH, inorganic ions, organic matter and H_2O_2 on *E. Coli* K12 photocatalytic inactivation by TiO_2 implications in solar water disinfection, Appl. Catal. B 51 (2004) 283–302, https://doi.org/10.1016/j.apcatb.2004.03.007.
[50] H. Xu, N. Roberts, F. Singleton, R. Attwell, D. Grimes, R. Golwell, Survival and viability of nonculturable *Escherichia coli* and *Vibrio cholerae* in the estuarine and marine environment, Microb. Ecol. 8 (1982) 313–323, https://doi.org/10.1007/BF02010671.
[51] X. Zeng, S. Lan, I.M.C. Lo, Rapid disinfection of *E. coli* by a ternary $BiVO_4$/Ag/g-C_3N_4 composite under visible light: photocatalytic mechanism and performance investigation in authentic sewage, Environ. Sci. Nano 6 (2019) 610–623, https://doi.org/10.1039/C8EN01283K.
[52] S. Huang, Y. Xu, M. Xie, Y. Ma, J. Yan, Y. Li, Y. Zhao, H. Xu, H. Li, Multifunctional C-doped $CoFe_2O_4$ material as cocatalyst to promote reactive oxygen species generation over magnetic recyclable C-CoFe/Ag-AgX photocatalysts, ACS Sustain. Chem. Eng. 6 (2018) 11968–11978, https://doi.org/10.1021/acssuschemeng.8b02279.
[53] Y. Li, Y. Li, S. Ma, P. Wang, Q. Hou, J. Han, S. Zhan, Efficient water disinfection with Ag_2WO_4-doped mesoporous g-C_3N_4 under visible light, J. Hazard. Mater. 338 (2017) 33–46, https://doi.org/10.1016/j.jhazmat.2017.05.011.
[54] Y. Deng, L. Tang, G. Zeng, Z. Zhu, M. Yan, Y. Zhou, J. Wang, Y. Liu, J. Wang, Insight into highly efficient simultaneous photocatalytic removal of Cr(VI) and 2,4-diclorophenol under visible light irradiation by phosphorus doped porous ultrathin g-C_3N_4 nanosheets from aqueous media: Performance and reaction mechanism, Appl. Catal. B 203 (2017) 343–354, https://doi.org/10.1016/j.apcatb.2016.10.046.
[55] V. Maroga Mboula, V. Hequet, Y. Andres, L.M. Pastrana Martinez, J.M. Dona Rodriguez, A.M. Silva, P. Falaras, Photocatalytic degradation of endocrine disruptor compounds under simulated solar light, Water Res. 47 (2013) 3997–4005, https://doi.org/10.1016/j.watres.2013.01.055.
[56] Q. Wang, M. Chen, G. Shan, P. Chen, S. Cui, S. Yi, L. Zhu, Bioaccumulation and biomagnification of emerging bisphenol analogues in aquatic organisms from Taihu Lake, China, Sci. Total Environ. 598 (2017) 814–820, https://doi.org/10.1016/j.scitotenv.2017.04.167.
[57] Z. Liang, X. Bai, P. Hao, Y. Guo, Y. Xue, J. Tian, H. Cui, Full solar spectrum photocatalytic oxygen evolution by carbon-coated TiO_2 hierarchical nanotubes, Appl. Catal. B 243 (2019) 711–720, https://doi.org/10.1016/j.apcatb.2018.11.017.
[58] L.K. Dhandole, M.A. Mahadik, S.G. Kim, H.S. Chung, Y.S. Seo, M. Cho, J.H. Ryu, J.S. Jang, Boosting photocatalytic performance of inactive rutile TiO_2nanorods under solar light irradiation: Synergistic effect of acid treatment and metal oxide co-catalysts, ACS Appl. Mater. Interfaces 9 (2017) 23602–23613, https://doi.org/10.1021/acsami.7b02104.
[59] B. Chai, T. Peng, X. Zhang, J. Mao, K. Li, X. Zhang, Synthesis of C_{60}-decorated SWCNTs (C_{60}-d-CNTs) and its TiO_2-based nanocomposite with enhanced photocatalytic activity for hydrogen production, Dalton Trans. 42 (2013) 3402–3409, https://doi.org/10.1039/c2dt32458j.
[60] C. Mercado, Z. Seeley, A. Bandyopadhyay, S. Bose, J.L. McHale, Photoluminescence of dense nanocrystalline titanium dioxide thin films: effect of doping and thickness and relation to gas sensing, ACS Appl. Mater. Interfaces 3 (2011) 2281–2288, https://doi.org/10.1021/am2006433.
[61] R.E. Rex, Y. Yang, F.J. Knorr, J.Z. Zhang, Y. Li, J.L. McHale, Spectroelectrochemical photoluminescence of trap states in H-treated rutile TiO_2 nanowires: implications for photooxidation of water, J. Phys. Chem. C 120 (2016) 3530–3541, https://doi.org/10.1021/acs.jpcc.5b11231.
[62] Y.J. Park, J.H. Oh, N.S. Han, H.C. Yoon, S.M. Park, Y.R. Do, J.K. Song, Photoluminescence of band gap states in $AgInS_2$ nanoparticles, J. Phys. Chem. C 118 (2014) 25677–25683, https://doi.org/10.1021/jp5102253.
[63] Y. Hamanaka, T. Ogawa, M. Tsuzuki, T. Kuzuya, Photoluminescence properties and its origin of $AgInS_2$ quantum dots with chalcopyrite structure, J. Phys. Chem. C 115 (2011) 1786–1792, https://doi.org/10.1021/jp110409q.
[64] X. Ma, Q. Xiang, Y. Liao, T. Wen, H. Zhang, Visible-light-driven CdSe quantum dots/graphene/TiO_2 nanosheets composite with excellent photocatalytic activity for *E. coli* disinfection and organic pollutant degradation, Appl. Surf. Sci. 457 (2018) 846–855, https://doi.org/10.1016/j.apsusc.2018.07.003.
[65] A. Kubacka, M.J. Muñoz Batista, M. Ferrer, M. Fernández Garcia, Er-W codoping of TiO_2-anatase: structural and electronic characterization and disinfection capability under UV–vis, and near-IR excitation, Appl. Catal. B 228 (2018) 113–129, https://doi.org/10.1016/j.apcatb.2018.01.064.
[66] A. Kubacka, M.J. Muñoz-Batista, M. Ferrer, M. Fernández-García, UV and visible light optimization of anatase TiO_2 antimicrobial properties: surface deposition of metal and oxide (Cu, Zn, Ag) species, Appl. Catal. B 140–141 (2013) 680–690, https://doi.org/10.1016/j.apcatb.2013.04.077.
[67] I. Nakamura, N. Negishi, S. Kutsuna, T. Ihara, S. Sugihara, K. Takeuchi, Role of oxygen vacancy in the plasma-treated TiO_2 photocatalyst with visible light activity for NO removal, J. Mol. Catal. A Chem. 161 (2000) 205–212, https://doi.org/10.1016/S1381-1169(00)00362-9.
[68] F. Li, X. Wang, Y. Zhao, J. Liu, Y. Hao, R. Liu, D. Zhao, Ionic-liquid-assisted synthesis of high-visible-light-activated N–B–F-tri-doped mesoporous TiO_2 via a microwave route, Appl. Catal. B 144 (2014) 442–453, https://doi.org/10.1016/j.apcatb.2013.07.050.
[69] Y. Luo, B. Deng, Y. Pu, A. Liu, J. Wang, K. Ma, F. Gao, B. Gao, W. Zou, L. Dong, Interfacial coupling effects in g-C_3N_4/$SrTiO_3$ nanocomposites with enhanced H_2 evolution under visible light irradiation, Appl. Catal. B 247 (2019) 1–9, https://doi.org/10.1016/j.apcatb.2019.01.089.
[70] R. Wang, X. Kong, W. Zhang, W. Zhu, L. Huang, J. Wang, X. Zhang, X. Liu, N. Hu, Y. Suo, J. Wang, Mechanism insight into rapid photocatalytic disinfection of *Salmonella* based on vanadate QDs-interspersed g-C_3N_4 heterostructures, Appl. Catal. B 225 (2018) 228–237, https://doi.org/10.1016/j.apcatb.2017.11.060.